Beyond the Young-Laplace model for cluster growth during dewetting of thin films: Effective coarsening exponents and the role of long range dewetting interactions

Adi Constantinescu,[*] Leonardo Golubović,[†] and Artem Levandovsky
Department of Physics and Astronomy, West Virginia University, Morgantown, West Virginia 26506-6315, USA
(Received 11 June 2013; revised manuscript received 20 August 2013; published 9 September 2013)

Long range dewetting forces acting across thin films, such as the fundamental van der Waals interactions, may drive the formation of large clusters (tall multilayer islands) and pits, observed in thin films of diverse materials such as polymers, liquid crystals, and metals. In this study we further develop the methodology of the nonequilibrium statistical mechanics of thin films coarsening within continuum interface dynamics model incorporating long range dewetting interactions. The theoretical test bench model considered here is a generalization of the classical Mullins model for the dynamics of solid film surfaces. By analytic arguments and simulations of the model, we study the coarsening growth laws of clusters formed in thin films due to the dewetting interactions. The ultimate cluster growth scaling laws at long times are strongly universal: Short and long range dewetting interactions yield the same coarsening exponents. However, long range dewetting interactions, such as the van der Waals forces, introduce a distinct long lasting early time scaling behavior characterized by a slow growth of the cluster height/lateral size aspect ratio (i.e., a time-dependent Young angle) and by effective coarsening exponents that depend on cluster size. In this study, we develop a theory capable of *analytically* calculating these effective size-dependent coarsening exponents characterizing the cluster growth in the early time regime. Such a pronounced early time scaling behavior has been indeed seen in experiments; however, its physical origin has remained elusive to this date. Our theory attributes these observed phenomena to ubiquitous long range dewetting interactions acting across thin solid and liquid films. Our results are also applicable to cluster growth in initially very thin fluid films, formed by depositing a few monolayers or by a submonolayer deposition. Under this condition, the dominant coarsening mechanism is diffusive intercluster mass transport while the cluster coalescence plays a minor role, both in solid and in fluid films.

DOI: 10.1103/PhysRevE.88.032113 PACS number(s): 05.70.Ln, 89.75.Da, 68.55.−a

I. INTRODUCTION

In a classic quantum electrodynamics study [1], Casimir made a striking prediction that two perfectly reflecting parallel plates placed in vacuum will attract each other. This exotic phenomenon is due to the modification of the quantum electromagnetic field ground state ("zero point") energy of the free space produced by the presence of the plates. Casimir's discovery had a great intellectual impact on the developments of the theoretical understanding of other forces in nature, in particular of the van der Waals forces. This deep understanding of the van der Waals forces was provided by Lifshitz, who related these forces to electronic charge density fluctuations existing in any material even at zero absolute temperature due to quantum effects [2,3]. These charge fluctuations and the induced electromagnetic field fluctuations generate transient dipole moments in atoms and produce effective forces acting even between neutral atoms. At zero temperature these forces are called London forces. Hamaker considered this London-van der Waals interaction in thin films [4]. He found that opposite surfaces of a thin film interact through the effective potential,

$$\Phi(h) = -\frac{A_H}{12\pi h^2}, \tag{1.1}$$

per unit area, where h is the thickness of the thin film and A_H is the so called Hamaker constant that can be calculated from the Lifshitz theory [2,3]. The potential $\Phi(h)$ is essentially a finite size contribution to the thin film net free energy. Van der Waals force is just one of a large number of potentially interesting thin film interactions; see, e.g., Refs. [4–6]. For example, in Ref. [7], it has been suggested that the opposite surfaces of smectic liquid crystal films interact with each other by an effective interaction inversely proportional to the film thickness,

$$\Phi(h) \sim -\frac{1}{h}. \tag{1.2}$$

This long range interaction is a thermomechanical quasi-Casimir force induced by smectic thermal undulations.

Ever since the seminal studies of Lifshits and Slyozov, and, independently, of Wagner [8], coarsening processes have played a prominent role in statistical [9] and biological physics [10] and in applied physical sciences [11–17]. Technologically significant thin films are no exception to this, as exemplified by growing microstructures seen in epitaxial growth [11,14]. A new venue in this area emerged from recent experimental revelations that long range dewetting forces acting across thin films, such as the above discussed van der Waals interactions [18], may induce the formation of large clusters, i.e., tall multilayer islands formed during high temperature annealing of thin films, [19]. Earlier experiments with liquid Sn [13] and solid Mn films [15] on silicon evidence that the clusters grow in time by a coarsening process, with cluster linear size $\sim t^{1/4}$ (at long times t), as predicted by Chakraverty [16,17]. However,

[*]Present address: Asia Pacific Center for Theoretical Physics, Hogil Kim Memorial Bldg., POSTECH San 31 Hysa-dong, Namgu, Pohang Gyeongbuk 790-784, South Korea.
[†]Corresponding author: lgolubov@wvu.edu

a more complex mode of cluster growth has also been seen, in solid Co films on sapphire [20]. In addition, an intriguing long lasting early time cluster growth behavior, preceding the $t^{1/4}$ regime, has been seen in the experiments [13].

In this study we further develop the methodology of the nonequilibrium statistical mechanics of thin films coarsening within continuum interface dynamics models incorporating dewetting interactions. The theoretical test bench model considered here is a generalization of the classical Mullins model for the dynamics of solid film surfaces [21]. Yet, under the conditions discussed in Sec. II E, our main results are *also* applicable to fluid films. By analytic arguments and simulations, we study the growth of clusters formed due to dewetting interactions, such as the common van der Waals and other experimentally significant long range interactions noted above. We extract the *effective (time-dependent) coarsening exponents* describing the cluster growth, such as the exponent

$$\beta_{\langle H\rangle}(t) = \frac{d\ln(\langle H\rangle)}{d\ln(t)}, \tag{1.3}$$

characterizing the growth of the cluster average height $\langle H\rangle$. For three-dimensional (3D) clusters on 2D substrates, this exponent approaches $1/4$ in long times limit, in accord with the experiments [13,15] and previous theories [16,17]. However, we reveal that long range (power-law) dewetting interactions introduce a long lasting *early time* scaling behavior characterized by effective cluster height growth exponent $\beta_{\langle H\rangle}(t)$ larger than $1/4$. Such a long lasting crossover behavior, with a $\beta_{\langle H\rangle}(t) \approx 0.33 > 1/4$, was indeed seen in the experiments [13], and its physical origin has remained elusive to this date. We show that such long lasting crossover phenomena can be produced by long range dewetting interactions discussed above, which are of the asymptotic form,

$$\Phi(h) \sim -\frac{1}{h^{\omega}}, \tag{1.4}$$

for large film thickness h. Note that Eqs. (1.1) and (1.2) correspond to Eq. (1.4) with $\omega = 2$ and $\omega = 1$, respectively. We theoretically prove, by numerical simulations and analytic methods, that the long range nature of dewetting forces indeed produces long lasting early time departures from the asymptotic power laws, with the effective exponent $\beta_{\langle H\rangle}(t) > 1/4$. This early time cluster growth regime is shown here to be marked by a growing cluster height-to-width aspect ratio which slowly approaches the aspect ratio determined by the Young contact angle. In this respect, notable are the experiments of Ref. [20], in which the clusters are indeed seen to exhibit a growing cluster aspect ratio. For realistic dewetting potentials, such as van der Waals and other long range interactions, these early time scaling phenomena are found here to persist over long intervals of time and they are thus experimentally significant.

The structure of this paper is as follows. In Sec. II, with due care for physics, we discuss the continuum modeling of the morphology dynamics of solid and liquid thin films. In this section we also outline a simple kinetic theory of the coarsening dynamics of the clusters formed during dewetting process. This discussion, however, provides the values of the cluster growth exponents (such as the above mentioned exponent β_H) that are valid only in the long times limit. In this limit, the clusters are large and can be simply described by the classical Young-Laplace model. We stress that all previous analytic studies of the cluster coarsening dynamics (starting with the seminal work of Chakraverty [16]) have been exclusively based on the Young-Laplace model for cluster morphology. *Our study, however, goes beyond the classical Young-Laplace model*. Thus, in Sec. III, we use numerical simulations of our interface dynamics model to explore the role played by the long range dewetting interactions on the character of the cluster coarsening dynamics. We find that these interactions produce significant early time departures from the asymptotic predictions based on the Young-Laplace model. To analytically address this phenomenon, in Sec. IV, we first provide a theoretical description of quasistatic (slowly evolving) clusters that goes beyond the classical Young-Laplace model. Next, in Sec. V, we use this theoretical description to develop a powerful cluster coarsening dynamics theory capable of analytically explaining the findings of our simulations. Finally, at the end we provide a summary and conclusion of this study. Some details relevant for our discussions are outlined in Appendixes A and B.

II. INTERFACE DYNAMICS MODELS WITH DEWETTING INTERACTIONS

A. Generalized Mullins model for solid films with dewetting potentials

Continuum modeling of solid film interfacial dynamics dates back to early works of Mullins and Herring [21]. In this section we discuss a basic model for solid film morphology dynamics respecting the conservation of the film volume of the general form [11,21]

$$\frac{\partial h}{\partial t} = -\vec{\nabla}\cdot\vec{J}. \tag{2.1}$$

Here, $h(\vec{x},t)$ is the film interface height over a D-dimensional substrate plane, $\vec{x} = (x_1, x_2, \ldots, x_D)$. In Eq. (2.1), $\vec{J}$ is the surface current density [21], given by the Nernst-Einstein equation,

$$\vec{J} = -\Gamma\vec{\nabla}\mu = -\Gamma\Omega\vec{\nabla}P. \tag{2.2}$$

Here, Γ is a transport coefficient, and μ is chemical potential field; $\mu(\vec{x},t) = \Omega P(\vec{x},t)$, with Ω, the atomic volume. Within the small slope approximation (SSA), $m = |\vec{\nabla}h| \ll 1$, the pressure field $P(\vec{x},t)$ in Eq. (2.2) is generated by the surface contribution to the film free energy, of the form [3,18]

$$F = \int d^D x \left[\frac{\gamma}{2}(\vec{\nabla}h)^2 + \Phi(h)\right], \tag{2.3a}$$

via the relation

$$P(\vec{x},t) = \frac{\mu(\vec{x},t)}{\Omega} = \frac{\delta F}{\delta h(\vec{x},t)} = -\gamma\vec{\nabla}^2 h + \Phi'(h). \tag{2.3b}$$

Above, γ is the interface stiffness of the film at its top interface with vacuum (or air), whereas $\Phi(h)$ is the dewetting interaction potential. As discussed in the Introduction, major physically interesting dewetting potentials have the asymptotic form of a power-law attraction,

$$\Phi(h) \sim -\frac{1}{h^{\omega}}, \tag{2.4}$$

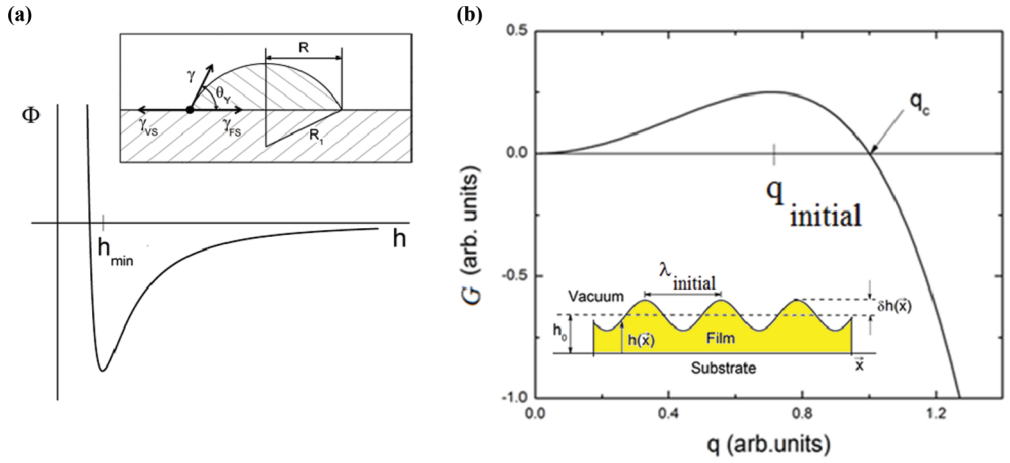

FIG. 1. (Color online) (a) Dewetting interaction potential causing the flat film instability. (Inset) Sketch of a cluster on top of a substrate depicting the Young-Dupré model of dewetting; γ, γ_{FS}, and γ_{VS} are the interface energies at vacuum-film, film-substrate, and vacuum-substrate interfaces, respectively; θ_Y is the cluster-substrate contact angle and R_1 is the radius of the curvature of the cluster interface with vacuum, whereas R is the radius of the cluster circular base. (b) Variation of the dispersion relation $G(q)$ as function of the magnitude of the wave vector q. (Inset) Schematic view of small fluctuations δh of the thin film surface around average thickness h_0.

for large h; see Fig. 1(a). The common nonretarded van der Waals interactions correspond to the case $\omega = 2$ of Eq. (2.4), [3]. The case $\omega = 1$ may also be interesting [7]. Short range dewetting interactions are regained in the large-ω limit; $\omega \gg 1$. By Eqs. (2.1)–(2.3),

$$\frac{\partial h}{\partial t} = \Gamma\Omega\vec{\nabla}^2 P = -\Gamma\Omega\vec{\nabla}^2[\gamma\vec{\nabla}^2 h - \Phi'(h)]. \qquad (2.5)$$

For $\Phi(h) = 0$, Eq. (2.5) reduces to the classical Mullins model for solid interface relaxation by surface diffusion [21], with the transport coefficient $\Gamma = \mu_{FV} n_{\rm surf}\Omega$. Here, $n_{\rm surf}$ is the surface density of surface active atoms and μ_{FV} is their mobility constant at the film-vacuum (or air) interface. Such a Mullins type model, emerging from a *seemingly* liquidlike surface free energy (2.3a), has already been employed by a number of authors to discuss some dewetting phenomena in solid films, [22,23]. As in these previous studies, we assume that the interface stiffness γ is positive. Thus, in the absence of dewetting potentials, an initially flat uniform film surface is stable against tilting. Within the SAA, the surface free energy [Eq. (2.3a)] is liquidlike. In fact, for the interesting crystal surfaces, such as (001) surface, the crystal anisotropy would show up only in higher order (quartic in slope) contributions to the interface free energy, so, within the SSA, it is sufficient to keep in Eq. (2.3a) just the isotropic term quadratic in slope. The higher order slope terms would be needed only if the γ in (2.3a) is negative, in which case the interface would develop tilted facets stabilized by the higher order terms. For a positive γ, however, the tilted facets do not develop and the anisotropy plays only a minor role. We note that the above model does not account for destabilizing elastic effects induced in some solid films by the substrates, such as the Asaro-Tiller-Grinfeld effect [24] or the formation of mounds in Si-Ge heteroepitaxial systems [25]. The substrate induced uniform film stress is, however, known to be vanishing if the substrate is incommensurate with the film along their interface. This is a rather common case for many thin film systems. Under such conditions, the only source of the uniform film instability in this model is the dewetting potential $\Phi(h)$; see Sec. II B. On the theoretical side, a conceptual advantage of dealing with such a simple model is that the actual physical effects of dewetting potentials are better highlighted. It should be also stressed that the classical Mullins model (2.5), with underlying liquidlike free energy (2.3a), effectively ignores the layered character of solids, i.e., their long range positional order. Because of this, in the applications to singular crystal surfaces, one would have to add to the free energy (2.3a) the oscillatory term of the form

$$F_{\rm positional} \sim -\int d^D x \cos\left(\frac{2\pi}{a} h(\vec{x},t)\right),$$

reflecting the crystal periodicity along the h axis [26]. For $D = 1$, singular surfaces are rough at any temperature and the above oscillatory interaction is renormalized to zero due to thermal fluctuations. For $D = 2$, such a dramatic renormalization occurs only above the roughening temperature $T_{\rm R}$, which is typically above the crystal melting temperature for low Miller index singular surfaces (with notable exception of solid He). Yet, the simple Mullins model is still in broad use in materials science studies of solid surfaces, including the studies of dewetting phenomena (e.g., Refs. [22,23]). Its predictions agree with numerous experiments (some of them done by Mullins himself and his collaborators [21]). The apparent success of the Mullins model can be attributed to the fact that realistic crystal surfaces, such as the surfaces of growing clusters, deviate significantly from a perfect singular surface structure. They are better described as miscut (vicinal) surfaces, and, under some conditions, Eqs. (2.3a) through (2.5) may become a viable phenomenological model even below $T_{\rm R}$. Such surfaces are always thermally rough in $D = 2$. Their thermal disorder may depress the effects of crystal periodicity. Within the Mullins model, dewetting is a continuous, nucleation free process which goes on in a swift way; see Sec. III simulations. Thermal effects, chemical disorder [15], or ion beam irradiation [28] may all produce a significant surface disorder and thus make the Mullins

model viable. Surface disorder should have similar dephasing effects on oscillatory surface potentials. Significant examples are the so-called fermionic Casimir potentials emerging from quantum size effects of traveling fermions such as conducting electrons in metallic films [5,6,27] of the form

$$\Phi_{\text{fermionic}}(h) \sim \frac{1}{h^{\alpha}} \cos(2k_{\text{Fermi}}h).$$

At low temperatures, such oscillatory fermionic Casimir forces are believed to induce the formation of small islands on singular surfaces [27]. We are, however, here interested in larger surface structures such as the clusters formed during a high temperature annealing of thin solid and liquid films [13,15,20], sometimes assisted by ion beam irradiation [28]. In the presence of thermal or other surface disorder, the oscillatory potentials may decohere and average out to zero, possibly giving rise to some effective induced dewetting potentials of the simple power-law form [Eq. (2.4)] considered in this paper. On the other hand, the surface disorder can never produce such dramatic effects on the monotonous (nonoscillatory) London-van der Waals dewetting potential in thin films.

As it stands, the model Eq. (2.5) only describes the dynamics of the film-vacuum(air) interface. It is thus applicable to multilayer regions with $h(\vec{x},t)/a > 1$ with $a =$ atomic monolayer height. Dewetting processes, however, involve the formation of "dry" submonolayer regions with $h(\vec{x},t)/a < 1$, where the film material disperses into a fluid (gas) of adatoms. In these regions, the physical meaning of the $h(\vec{x},t)$ field is expressed by the relation

$$h(\vec{x},t) = \Omega n(\vec{x},t), \tag{2.6}$$

where $n(\vec{x},t)$ is the local surface number density of adatoms diffusing on the substrate: By the relation (2.6), the integral of the $h(\vec{x},t)$ field over any submonolayer domain is equal to the total film material volume over the submonolayer domain. Thus, the relation (2.6) manifestly preserves the major conceptual feature of the h field that the integral of $h(\vec{x},t)$ over *any* substrate domain is equal to the total film material volume over this domain. By means of the concept encoded in Eq. (2.6), the above discussed multilayer Mullins model (2.5) can be generalized to address the submonolayer regions with $h(\vec{x},t)/a < 1$. In these regions, the free energy functional Eq. (2.3a) needs to be replaced by the free energy density functional of the fluid of adatoms with local density $n(\vec{x},t) = h(\vec{x},t)/\Omega$. In general, free energy functionals can be expressed as expansions in powers of spatial derivatives of the involved fields. Hence, for our problem, the minimally needed free energy functional can be written as

$$F_{\text{eff}} = \int d^D x \left[\frac{\gamma(h)}{2} (\vec{\nabla} h)^2 + \Phi_{\text{eff}}(h) \right]. \tag{2.7}$$

With suitable forms of the *effective* local potential $\Phi_{\text{eff}}(h)$ and the *stiffness function* $\gamma(h)$, the functional Eq. (2.7) can be used to treat the situations with both $h(\vec{x},t)/a > 1$ and $h(\vec{x},t)/a < 1$ in a *unified* way. For multilayer domains with $h(\vec{x},t)/a > 1$, the effective local potential $\Phi_{\text{eff}}(h)$ reduces to the dewetting potentials discussed in Sec. I, while the stiffness function obeys the limit $\gamma(h \to \infty) \to \gamma$, where γ is the stiffness of the film interface with vacuum (or air). On the other side, for submonolayer domains with $h(\vec{x},t)/a < 1$, Eq. (2.7) should reduce to the free energy density functional of the fluid of adatoms with local density $n(\vec{x},t) = h(\vec{x},t)/\Omega$. For example, for $h(\vec{x},t)/a \ll 1$, whence the adatom gas is dilute and can be treated as an ideal gas, one can apply the familiar results for ideal gasses to write

$$\begin{aligned} \Phi_{\text{eff}}(h) &\approx \Phi_{\text{eff}}(0) + k_B T n \ln\left(\frac{n}{e n_o}\right) \\ &= \Phi_{\text{eff}}(0) + k_B T \frac{h}{\Omega} \ln\left(\frac{h}{e\Omega n_o}\right), \end{aligned} \tag{2.8}$$

where n_o is a reference gas density. If the adatom gas is uniform, the resulting chemical potential implied by Eq. (2.8) has the familiar ideal gas form

$$\begin{aligned} \mu &= \frac{\partial \Phi_{\text{eff}}}{\partial n} = \Omega \cdot \Phi'_{\text{eff}}(h) \approx k_B T \ln\left(\frac{n}{n_o}\right) \\ &= k_B T \ln\left(\frac{h}{\Omega n_o}\right). \end{aligned} \tag{2.9}$$

By Eq. (2.9), the effective potential $\Phi_{\text{eff}}(h)$ must be a decreasing function for small $h = \Omega n$, whence the ideal gas model becomes exact. On the other side, for $h(\vec{x},t) \gg a$, whence $\Phi_{\text{eff}}(h)$ reduces in form to a dewetting potential as in Eq. (2.4), the $\Phi_{\text{eff}}(h)$ is expected to be an increasing function of h. By these observations, one arrives at a simple yet very important general conclusion that the $\Phi_{\text{eff}}(h)$ must have a minimum at a characteristic value of h, called $h_{\min}$ in Fig. 1(a), at which the (uniform adatom fluid) chemical potential $\mu = \Omega \cdot \Phi'_{\text{eff}}(h)$ vanishes. The $h_{\min}$ corresponds to the adatom gas density $n_{\min} = h_{\min}/\Omega$, which is the equilibrium density of the adatom gas coexisting with a macroscopic wedge shaped film; see Sec. II C and Appendix A. For a spatially nonuniform $h(\vec{x},t)$, the chemical potential and pressure fields are obtained via the functional derivative of the unified free energy functional Eq. (2.7), with the result

$$\begin{aligned} P(\vec{x},t) &= \frac{\mu(\vec{x},t)}{\Omega} = \frac{\delta F_{\text{eff}}}{\delta h(\vec{x},t)} \\ &= -\vec{\nabla}[\gamma(h)\vec{\nabla}h] + \frac{1}{2}\gamma'(h)(\vec{\nabla}h)^2 + \Phi'_{\text{eff}}(h) \\ &\equiv -\gamma(h)\vec{\nabla}^2 h - \frac{1}{2}\gamma'(h)(\vec{\nabla}h)^2 + \Phi'_{\text{eff}}(h), \end{aligned} \tag{2.10}$$

applicable for both $h(\vec{x},t)/a > 1$ and $h(\vec{x},t)/a < 1$ with suitably chosen forms of the effective local potential $\Phi_{\text{eff}}(h)$ and the stiffness function $\gamma(h)$. Note that the above form of the pressure field is more complex than that in Eq. (2.3b) because of taking into account the h dependence of the stiffness $\gamma(h)$. The above mentioned film wedge configuration is the equilibrium solution of Eq. (2.10) with zero chemical potential, $\mu = 0$. For this solution, away from the wedge, $h(\vec{x},t) \to h_{\min}$, that is, the adatom density $n(\vec{x},t) \to n_{\min} = h_{\min}/\Omega$. This feature can be used to calculate the Young contact angle for interfaces modeled by free energy functional Eq. (2.7); see Sec. II C and Appendix A. The chemical potential Eq. (2.10) can be used to discuss the dynamics of the solid film dewetting, in combination with Nernst-Einstein relation of the from

$$\vec{J} = -\Gamma(h)\vec{\nabla}\mu = -\Gamma(h)\Omega\vec{\nabla}P. \tag{2.11}$$

Here, $\Gamma(h)$ is an h-dependent transport coefficient discussed in the following. The conservation law Eq. (2.1) in combination with Eqs. (2.10) and (2.11) yields a generalized Mullins dynamical model of the form

$$\frac{\partial h}{\partial t} = -\vec{\nabla}\vec{J} = \vec{\nabla}[\Gamma(h)\vec{\nabla}\mu] = \Omega\vec{\nabla}[\Gamma(h)\vec{\nabla}P] = -\Omega\vec{\nabla}\left\{\Gamma(h)\vec{\nabla}\left[\gamma(h)\vec{\nabla}^2 h + \frac{1}{2}\gamma'(h)(\vec{\nabla}h)^2 - \Phi'_{\rm eff}(h)\right]\right\}. \tag{2.12}$$

To implement the model Eq. (2.12), we need the functional form of the transport coefficient $\Gamma(h)$. For $h(\vec{x},t) > a$ (i.e., in multilayer domain), the $\Gamma(h)$ should coincide with above mentioned Mullins result discussed below Eq. (2.5), that is

$$\Gamma_{\rm Mullins}(h) = \mu_{FV} n_{\rm surf}\Omega \sim \mu_{FV} a. \tag{2.13a}$$

So, for $h(\vec{x},t) > a$ the $\Gamma(h)$ is a nearly h-independent constant. On the other hand, for $h(\vec{x},t) < a$ (i.e., in submonolayer domain) one deals with a gas of adatoms and Eq. (2.6) applies. Then the appropriate form of $\Gamma(h)$ is

$$\Gamma(h) = \mu_{\rm sub} h, \tag{2.13b}$$

where $\mu_{\rm sub}$ is the mobility constant of adatoms diffusing on the substrate. Indeed, for $h(\vec{x},t) \ll a$, the generalized Mullins model Eq. (2.12), in combination with the effective potential in Eq. (2.8) and the transport coefficient in Eq. (2.13b), reduces (to the lowest order in spatial derivatives) to the simple diffusion equation

$$\frac{\partial h}{\partial t} = D_{\rm sub}(\vec{\nabla})^2 h, \tag{2.14}$$

with $D_{\rm sub} = k_B T \mu_{\rm sub}$. As $h(\vec{x},t) = \Omega n(\vec{x},t)$, by Eq. (2.14) we see that for $h(\vec{x},t) < a$ our general model Eq. (2.12) regains the standard diffusional dynamics expected for the gas of adatoms. The $\gamma(h)$ terms in the full dynamical model (2.12) produce only higher derivative terms that are subdominant to the leading diffusive term displayed in Eq. (2.14); see also Sec. II D discussions. We note that for $h(\vec{x},t) < a$, the physical origin of the $\gamma(h)$ term in the model free energy Eq. (2.7) is the interaction between adatoms, i.e., $\gamma(h)$ vanishes in ideal gasses of adatoms. Thus, if the adatom gas is dilute $[h(\vec{x},t) \ll a]$ or the temperature is high enough, the dominant role is played by the ideal gas entropic contribution to the model free energy density displayed in Eq. (2.8), whereas the $\gamma(h)$ term plays a more minor role in the full free energy Eq. (2.7). Still, the $\gamma(h)$ term cannot be ignored. For example, it is needed to develop a consistent continuum theory of the Young contact angle based on considering the wedge shaped film profiles; see Sec. II C.

Mathematically, the generalized Mullins model (2.12) is similar to the models for the dewetting dynamics of liquid thin films [29–32]. For liquid films, however, the interface dynamics is mediated by the hydrodynamic flows in the bulk of the film, in contrast to the Mullins model in which only the atoms on the interface contribute to its dynamics. Related to this, the transport coefficients of the liquid films models [29–32] depend profoundly on the local film thickness, as $\Gamma(h) \sim h^q$, with, for example, $q = 3$, for the no-slip boundary conditions at fluid-substrate interface. In contrast to this, the generalized Mullins model has a nearly constant $\Gamma(h)$ in the multilayer regions [Eq. (2.13a)]. Nonetheless, as discussed at the end of Sec. II E, our main results are also applicable to initially very thin fluid films whence the dominant coarsening mechanism is diffusive intercluster mass transport while the cluster coalescence plays a minor role. Thus, under these conditions, our major results for the generalized Mullins model (described in Secs. III, IV, and V) are also applicable to the coarsening in fluid thin films.

B. Thin film instability

The presence of the dewetting effective potential $\Phi_{\rm eff}(h)$ in the model (2.12) may induce an undulational (spinodal dewetting) instability of flat ($h = const.$) films similar to that occurring in liquid thin films [29]. To exhibit its presence in the Mullins model for solid films, consider a thin film of average thickness h_0, with a small undulational fluctuation $\delta h(\vec{x},t)$,

$$h(\vec{x},t) = h_0 + \delta h(\vec{x},t) = h_0 + A_{\vec{q}}(t)\cos(i\vec{q}\vec{x}),$$

with $\delta h \ll h_0$, as depicted in Fig. 1(b) inset. By linearizing Eq. (2.12) one easily finds $A_{\vec{q}}(t) = A_{\vec{q}}(0)\exp[G(q)t]$, with the dispersion relation $G(q)$ given by

$$G(q) = \Gamma(h_0)\Omega\cdot[-\gamma(h_0)q^4 - q^2\Phi''_{\rm eff}(h_0)]. \tag{2.15}$$

This result is essential for understanding of the initiation of the thin film dewetting process. If $\Phi''_{\rm eff}(h_0) > 0$, the $G(q)$ is negative for any $\vec{q}$, and the fluctuations of the film about the initial thickness h_0 will smooth out. The flat film is thus stable. On the other hand, as depicted in Fig. 1(b), if $\Phi''_{\rm eff}(h_0) < 0$, the $G(q)$ is positive in the range $|\vec{q}| < q_c$, with $q_c = \sqrt{-\Phi''_{\rm eff}(h_0)/\gamma(h_0)}$. The fluctuations with $|\vec{q}| < q_c$ grow exponentially in time, making the film interface unstable. This instability initiates the dewetting of the thin film. In this initiation, the dominant role is played by the fastest growing fluctuations, with the largest value of $G(q)$ corresponding to its maximum seen in Fig. 1(b). Their wave vector $q_{\rm initial}$ can easily be evaluated from the condition $G'(q_{\rm initial}) = 0$ yielding $q_{\rm initial} = q_c/\sqrt{2}$, corresponding to the wavelength

$$\lambda_{\rm initial} = \frac{2\pi}{q_{\rm initial}} = 2\pi\sqrt{\frac{2\gamma(h_0)}{-\Phi''_{\rm eff}(h_0)}}. \tag{2.16}$$

The corresponding value of the dispersion relation Eq. (2.15) is

$$G(q_{\rm initial}) = \Gamma(h_0)\Omega\cdot\frac{[\Phi''_{\rm eff}(h_0)]^2}{4\gamma(h_0)}. \tag{2.17}$$

The reciprocal of $G(q_{\rm initial})$ is the characteristic time scale for the growth of the spinodal decomposition instability. Due to the spinodal instability, the thin film structures into a periodiclike pattern with wavelength $\lambda_{\rm initial}$, see Fig. 1(b) inset. As the film continues to evolve, it will subsequently form arrays of pits, as exemplified by our simulations discussed in Sec. II D. These arrays of pits are, however, unstable and subsequently transform into arrays of cluster. The initial separation between these clusters is $\sim \lambda_{\rm initial}$. These clusters continue to grow via a coarsening process discussed in the following sections. In the context of solid films, spinodal dewetting was observed in Cr films [33], as well as in the smectic liquid crystal films [34]. Smectics are one-dimensionally periodic solids

and their observed spinodal dewetting may be induced by the potential in Eq. (1.2) [7]. It should be stressed that the fast spinodal instability in solid films may be induced only in the situations when the Mullins model is applicable; recall the positional order effects discussed below Eq. (2.5). They may (meta)stabilize singular crystal surfaces below the roughening transition temperature. Dewetting and cluster formation in such situations will still occur, however, after a long nucleation time. On the other hand, the miscut (vicinal) surfaces and other surfaces with a significant disorder may undergo swift spinodal instability induced by dewetting potentials [see the discussion below Eq. (2.5)]. It should be also noted that dewetting and cluster formation can also be swiftly initiated if the initial film is in a submonolayer state, as in the experiments of Ref. [15].

C. Young contact angle

Due to the presence of clusters, at long times the film partially "dewets": Large slowly growing (quasistatic) clusters sitting on "dry" substrate area are formed; see Fig. 1(a). The "dry area" corresponds to the minimum $\Phi_{\min}$ of the effective potential $\Phi_{\rm eff}(h)$, at $h_{\min}$(∼atomic size) in Fig. 1(a). In the limit of very large clusters, the cluster pressure $P \to 0$; see Sec. II E in the following. In this limit, the *maximum* cluster profile slope [occurring close to cluster base at an inflection point of cluster radial profile] $m_{\max} = \tan(\theta_{\max}) = |\vec{\nabla} h|_{\max}$ approaches the Young contact angle slope $m_Y = \tan(\theta_Y)$. The calculation of the Young angle has been discussed in literature, e.g., in the works of De Gennes and co-workers [18]. These works have, however, assumed that the stiffness function $\gamma(h)$ in the free energy functional (2.7) is simply a constant equal to the stiffness of the film interface with vacuum (or air). This is a (nearly) valid assumption for the multilayered film region, however, it badly breaks down once the submonolayer region is incorporated into the unified model, as we discussed in Sec. II A. Therefore, in our Appendix A we present Young angle calculation for the more general free energy model Eq. (2.7) discussed in Sec. II A, with an h-dependent stiffness $\gamma(h)$. The result is given by

$$m_Y = \tan(\theta_Y) = \sqrt{\frac{-2\Phi_{\min}}{\gamma}}, \tag{2.18}$$

where $\gamma = \lim_{h\to\infty} \gamma(h)$, is the stiffness of the film-vacuum interface (far away from the contact point). Interestingly, by the derivation of Eq. (2.18) presented in Appendix A, one arrives at a nontrivial conclusion that the Young contact angle does *not* depend on the detailed functional form of the height-dependent stiffness $\gamma(h)$. This has *not* been noted in the previous studies [18]. We stress that the result Eq. (2.18) for the Young contact angle actually applies to large clusters in any D, see Appendix A. It is physically illuminating to note that, within the SSA, Eq. (2.18) is closely related to the standard Young-Dupré law,

$$\gamma \cos(\theta_Y) + \gamma_{FS} = \gamma_{VS}, \tag{2.19}$$

for the cluster-substrate contact angle θ_Y; see Fig. 1(a) inset. To see this, we note that the film-substrate surface tension γ_{FS} and vacuum-substrate surface tension γ_{VS} satisfy the relation

$$\gamma_{VS} - \gamma_{FS} - \gamma = \Phi_{\min} \equiv \Phi_{\rm eff}(h_{\min}), \tag{2.20}$$

suggested by de Gennes [18]. Within the SSA employed in the model, $\cos(\theta_Y) \approx 1 - \tan^2(\theta_Y)/2$, and, by Eq. (2.20), it is easy to see that Eqs. (2.18) and (2.19) are equivalent to each other. It should be stressed that the Young-Dupré law is valid only in the limit of very large clusters (see Appendix A). For finite size clusters, however, the effects of dewetting potentials become more significant and the Young-Dupré law is not applicable; see Sec. IV. This feature gives rise to the interesting phenomena we reveal in the following sections of this paper; see Secs. III, VI, and V.

D. Rescaled dynamical model and simulation procedure

By the discussions of Sec. II A, a realistic description of the dewetting of solid films should be based on the generalized Mullins model Eq. (2.12) employing h-dependent transport coefficient $\Gamma(h)$ and stiffness function $\gamma(h)$. The h dependence of $\Gamma(h)$ is, however, not dramatic. Over the submonolayer regions, $h \approx h_{\min} \sim a$, so by Eq. (2.13b), the $\Gamma(h) \approx \Gamma(h_{\min}) = \mu_{\rm sub} h_{\min} \sim \mu_{\rm sub} a$ is nearly constant throughout submonolayer regions. Likewise, for multilayer regions we have the Mullins result in Eq. (2.13a). By it, if $\mu_{FV} \sim \mu_{\rm sub}$, one has $\Gamma_{\rm Mullins} \sim \Gamma(h_{\min})$ so in a qualitative discussion one can set $\Gamma(h) = \Gamma(h_{\min}) = const.$ for any h. Moreover, as discussed in Sec. II E, the cluster coarsening dynamics is (under some conditions) dominated by intercluster mass transport over dry submonolayer areas (with $h \approx h_{\min}$) so setting $\Gamma(h) = \Gamma(h_{\min})$ is the appropriate choice. One is also tempted to set the stiffness function $\gamma(h)$ to be simply equal to its limit $\gamma(h \to \infty) \to \gamma$, where γ is the stiffness of the film-vacuum interface. This *ad hoc* choice has been commonly adopted in previous studies of liquid films dewetting [18,30–32], yet it certainly breaks down in submonolayer regions with $h < a$; see Sec. II A. Fortunately, the detailed behavior of $\gamma(h)$ for $h < a$ is somewhat secondary. For example, as shown in Appendix A, the value of Young contact angle does not depend on the detailed form of the height-dependent stiffness $\gamma(h)$. Rather, the Young angle depends only on $\gamma = \lim_{h\to\infty} \gamma(h)$. Another example is the submonolayer diffusive dynamics Eq. (2.14). The $\gamma(h)$ terms in the full dynamical model (2.12) produce only higher derivative terms that are subdominant to the leading diffusive term explicitly displayed in Eq. (2.14). Thus, within the submonolayer regions, the choice of $\gamma(h)$ is irrelevant as long as the h field exhibits only long length scale variations over the submonolayer regions between the clusters. This, however, turns out to be the case, so the *ad hoc* replacement of $\gamma(h)$ with $\gamma = \lim_{h\to\infty} \gamma(h)$ will yield a viable dynamical model.

In view of the above discussions, for the purpose of our numerical simulations, we considered the dynamical model (2.12) with constant transport coefficient and stiffness function, $\Gamma(h) = \Gamma$, $\gamma(h) = \gamma$. To explore the role of long range power low tails of the dewetting potential Eq. (2.4), we simulated the dynamical model in Eq. (2.12) with a model form of the local potential with

$$\Phi'_{\rm eff}(h) = \frac{A}{h^{\omega+1}} \left[1 - \left(\frac{h_{\min}}{h} \right)^{\omega} \right], \tag{2.21}$$

corresponding to the potential

$$\Phi_{\rm eff}(h) = -\frac{A}{\omega h^{\omega}}\left[1 - \frac{1}{2}\left(\frac{h_{\rm min}}{h}\right)^{\omega}\right], \qquad (2.22)$$

having minimum at $h_{\rm min}$, as in Fig. 1(a). With this $\Phi_{\rm eff}(h)$, by a simple rescaling of $(\vec{x},t,h)$, the continuum model stated in Eqs. (2.12) and (2.21) can be made dimensionless (with $\Gamma\Omega = \gamma = A = 1$), of the form

$$\frac{\partial h}{\partial t} = \vec{\nabla}^2 P = -\vec{\nabla}^2[\vec{\nabla}^2 h - \Phi'_{\rm eff}(h)], \qquad (2.23)$$

and

$$\Phi'_{\rm eff}(h) = \frac{1}{h^{\omega+1}}\left[1 - \left(\frac{h_{\rm min}}{h}\right)^{\omega}\right]. \qquad (2.24)$$

We chose the rescaling of the original model such that, in the rescaled model,

$$h_{\rm min} = \left(\frac{\omega+2}{2(2\omega+1)}\right)^{1/\omega}. \qquad (2.25)$$

This choice is a matter of future convenience. [Other choices, such as $h_{\rm min} = 1$, are also possible to achieve by the choice of rescaling. The choice in Eq. (2.25) is preferred because it gives a very simple form to Eq. (2.31) discussed in the following.]

The rescaled dynamical model in Eqs. (2.23)–(2.25) depends on a single parameter, the exponent ω of the power-law tail of the dewetting potential Eq. (2.4). To explore the role of this exponent (i.e., the interaction range), we have numerically simulated the model Eqs. (2.23)–(2.25) for three different ω values, $\omega = 1,2,$and 6. Quantitative results of these simulations are presented in Sec. III, whereas some qualitative results are displayed in Figs. 2 and 3 in this section. The interface evolution equation Eq. (2.23) is numerically solved by standard Euler algorithm,$\partial_t h(\vec{x},t) \to [h(\vec{x},t+\Delta t) - h(\vec{x},t)]/\Delta t$, with $\Delta t = 0.00390625$ for $\omega = 1$, $\Delta t = 0.0016$ for $\omega = 2$, and $\Delta t = 0.000377$ for $\omega = 6$. The initial condition at $t = 0$ is discussed in the following paragraph; see Eq. (2.32) in the following. For the purposes of Sec. III, ten statistically independent simulations ("samples") were done for each ω; each sample was run up to one million time steps. For $D = 2$ systems, Eq. (2.23) was solved on a simple square lattice which is an 800 × 800 grid with the lattice constant Δx. For comparison, we also simulated the $D = 1$ case on a lattice with 64 000 sites. The two Laplacians on the right hand side of Eq. (2.23) are numerically evaluated using the first order approximation,

$$\vec{\nabla}^2\Psi(\vec{x},t) \to \left[\sum_{nn}\Psi(\vec{x}_{nn},t) - 2D\cdot\Psi(\vec{x},t)\right] \Big/ (\Delta x)^2,$$

where the sum runs over the 2D nearest neighbor lattice sites $(\vec{x}_{nn})$ of the site $\vec{x}$. The chosen lattice constant $\Delta x = 0.707107$ for $\omega = 1$, $\Delta x = 0.565685$ for $\omega = 2$, and $\Delta x = 0.372134$ for $\omega = 6$. We note that these lattice constants are about 14 to 15 times smaller than the spinodal instability wavelength given by Eq. (2.16), which, for the simulated model in Eqs. (2.23)–(2.25), reduces to the simple expression $\lambda_{\rm initial} = 4\pi/\sqrt{\omega}$.

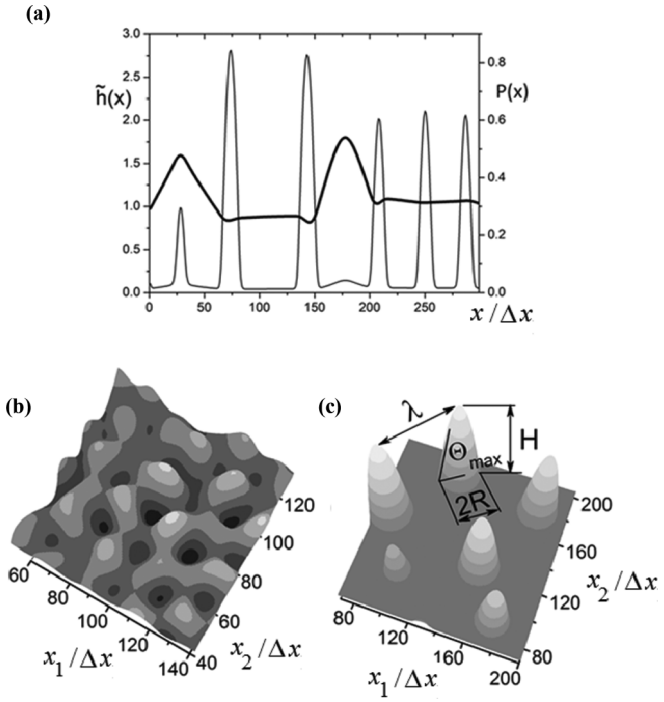

FIG. 2. (a) A snapshot from our simulations: The interface profile $\tilde{h}(x,t) = h(x,t) - h_{\rm min}$(thinner line) in $D = 1$ (with $\omega = 1$) and the corresponding field of pressure $P(x,t)$ (thicker line), at $t = 78.125$. Snapshots from our simulations in $D = 2$ (with $\omega = 1$): (b) at $t = 78.125$, showing the initial stage of the $D = 2$ thin film interface, dominated by the formation of pits; (c) at $t = 156.25$, showing the ultimate stage of the $D = 2$ thin film interface evolution, dominated by the presence of growing clusters.

By Eqs. (2.24) and (2.25), the rescaled model potential

$$\Phi_{\rm eff}(h) = -\frac{1}{\omega h^{\omega}}\left[1 - \frac{1}{2}\left(\frac{h_{\rm min}}{h}\right)^{\omega}\right] \qquad (2.26)$$

has a single inflection point,

$$\Phi''_{\rm eff}(h_{\rm inf}) = 0, \qquad (2.27)$$

at the height

$$h_{\rm inf} = \left(\frac{\omega+2}{2(\omega+1)}\right)^{1/\omega}. \qquad (2.28)$$

For the initial ($t = 0$) thin film interface heights $h(\vec{x},t = 0) = h_0$ that are above the inflection point, one has

$$\Phi''_{\rm eff}(h_0) < 0. \qquad (2.29)$$

Thus, by the Sec. II B discussion, such films are unstable and will undergo spinodal dewetting. Interestingly, among these unstable films there is one which is the most unstable. Indeed, Eq. (2.17) shows that by maximizing the magnitude of $\Phi''_{\rm eff}(h_0)$ one can minimize the time scale of the instability, i.e., maximize its rate. Thus, this maximization corresponds to the condition

$$\Phi'''_{\rm eff}(h_0) = 0 \qquad (2.30)$$

for the initial film height. By Eqs. (2.24) and (2.25), it is easy to show that Eq. (2.30) is solved by

$$h_0 = 1. \qquad (2.31)$$

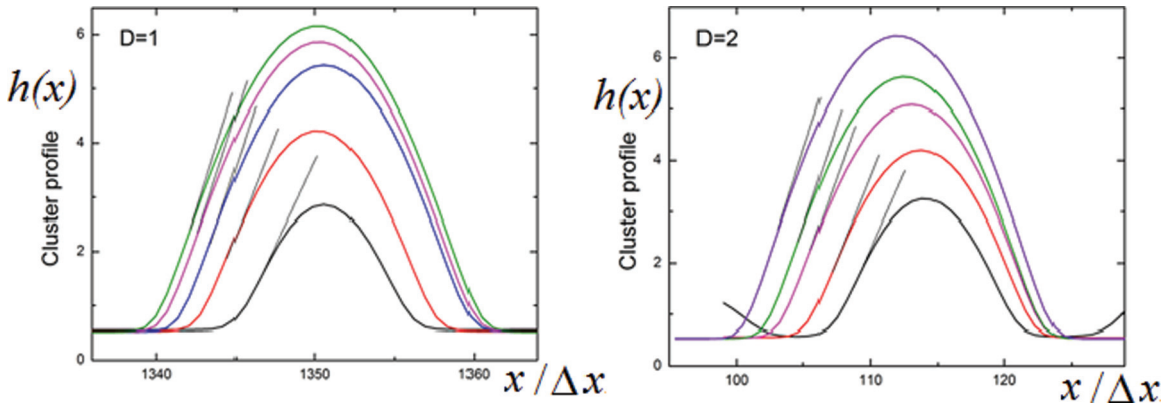

FIG. 3. (Color online) (Left) Interface height plots showing the formation of a slowly growing cluster for $D = 1$ and $\omega = 1$, from our simulation of the rescaled model with dimensionless t, $\vec{x}$, and h [as in Fig. 2(a)], at times $t = 2T$, $10T$, $30T$, $80T$, and $100T$. Here, $T = 39.0625 = 10^4\ \Delta t$. Well-structured clusters are seen for the first time at times $\sim T$. In the figure, we indicate tangents drawn at inflection points of the cluster profiles. Note that the tangent slope slowly grows in time. (Right) Interface height plots showing the formation of a slowly growing cluster for $D = 2$ and $\omega = 1$, from our simulation of the rescaled model with dimensionless t, $\vec{x}$, and h [as in Figs. 2(b) and 2(c)], at times $t = 10T$, $20T$, $40T$, $60T$, and $100T$. Here, again, $T = 39.0625 = 10^4\ \Delta t$. The time $\sim 3T$ corresponds to the crossover from pits arrays [seen in Fig. 2(b)] to cluster dominated surface morphology [seen in Fig. 2(c)]; see also Fig. 4(b). In the above figure, we indicate tangents drawn at inflection points of the cluster profiles. Note that the tangent slope slowly grows in time.

Motivated by this feature, in our simulations of the rescaled model, we set the initial height to be

$$h(\vec{x},t=0) = h_0 = 1 + \text{a small random field}, \quad (2.32)$$

to initiate the spinodal dewetting instability. The thin film satisfying Eq. (2.30) undergoes the fastest possible spinodal instability and quickly passes from the initial instability time stage to the stage characterized by cluster formation. It should be stressed that the initial condition in Eq. (2.32) was motivated by practical reasons, to avoid too much of our computation time spent on the relatively simple spinodal instability time stage. Our primary interest is in the postinstability stage when the clusters appear and grow; see Figs. 2(a) and 2(c) from our simulations. Quantitative simulation results from this ultimate, cluster dominated stage are presented and discussed in detail in Sec. III. In $D = 2$, this ultimate stage is preceded by an initial stage in which arrays of pits are formed; see Fig. 2(b) from our simulations.

At the minimum, the rescaled potential in Eq. (2.26) has the value

$$\Phi_{\min} = \Phi_{\text{eff}}(h_{\min}) = -\frac{2\omega+1}{\omega(\omega+2)}. \quad (2.33)$$

Thus, by Eqs. (2.33) and (2.18) [applied to the rescaled model with $A = \gamma = 1$], the Young angle slope for the rescaled model Eqs. (2.23)–(2.25) has the value

$$m_Y = \tan(\theta_Y) = \sqrt{\frac{2(2\omega+1)}{\omega(\omega+2)}}. \quad (2.34)$$

As discussed in Sec. II C and Appendix A, this result applies in the limit of large clusters. For a finite size cluster, the corresponding quantity is the *maximum* cluster slope $m_{\max} = \tan(\theta_{\max}) = |\vec{\nabla} h|_{\max}$ [occurring close to cluster base in Fig. 2(c), at an inflection point of cluster radial profile]. This slope is expected to approach the Young contact angle slope $m_Y = \tan(\theta_Y)$ in the limit of large clusters. This feature is illustrated in Fig. 3 from our simulations in which we display the tangents drawn at the inflection points on a growing cluster. One can see that the slope of these tangents indeed slowly grows as the cluster grows. This phenomenon plays a significant role in the discussions in the following sections.

E. Cluster coarsening dynamics in the Young-Laplace limit

In this section we qualitatively discuss the cluster formation and the laws of cluster coarsening growth by a simple kinetic scaling theory. More quantitative theory is developed in Sec. V; however, the discussions in this section will be useful to set the conceptual stage for this theory. Of direct interest is the case with substrate dimension $D = 2$. However, we consider these phenomena in a general number of dimensions. Thus, in the following, we are looking at $D + 1$-dimensional clusters on a D-dimensional substrate. The pressure field is nearly uniform within a cluster, $P(\vec{x},t) \approx P_{\text{cluster}}$, with each cluster having a different pressure, as exemplified by Fig. 2(a) from our simulations in $D = 1$. In this section, we consider clusters in the Young-Laplace limit (in any D). In this limit clusters are large and the cluster radial profile has the simple parabolic (spherical cap) form

$$h(r) \approx H\left[1 - \left(\frac{r}{R}\right)^2\right], \quad (2.35)$$

for $r < R =$ cluster base radius in Fig. 2(c), while

$$P_{\text{cluster}} \approx \frac{2D\gamma \cdot H}{R^2}. \quad (2.36)$$

Equations (2.35) and (2.36) are easily obtained by ignoring the potential $\Phi_{\text{eff}}(h)$ in Eq. (2.10) with $\gamma(h) = \gamma$. This reduces the equation to the simple Poisson equation

$$P_{\text{cluster}} \approx -\gamma \nabla^2 h, \quad (2.37)$$

spelling the classical Laplace relation between the pressure and the interface curvature. The potential $\Phi_{\text{eff}}(h)$, however,

does become important for $r \approx R$, where the cluster slope assumes the value of the Young angle slope Eq. (2.18). Thus, by Eq. (2.35),

$$m_Y = \tan(\theta_Y) = |h'(R)| \approx \frac{2H}{R}. \tag{2.38}$$

By Eqs. (2.38) and (2.36), the cluster pressure has the form

$$P_{\text{cluster}} \approx \frac{D\gamma m_Y^2}{2H} \approx \frac{D\gamma m_Y}{R}, \tag{2.39}$$

valid in the *Young-Laplace cluster model* based on Eqs. (2.35)–(2.38). By the conservation law Eq. (2.1), the cluster volume V_{cluster} changes in time according to the equation

$$\frac{d}{dt} V_{\text{cluster}} = -I. \tag{2.40}$$

Here, the I is the volume current discussed in the following, while, by Eq. (2.35),

$$V_{\text{cluster}} = S(D) \int_0^R dr r^{D-1} h(r) = \frac{2S(D)}{D(D+2)} H R^D. \tag{2.41}$$

Here $S(D)$ is the surface area of the D-dimensional unit sphere, given by the expression

$$S(D) = \frac{(2\pi)^{D/2} 2^{1-D/2}}{\bar{\Gamma}(D/2)}, \tag{2.42}$$

where $\bar{\Gamma}$ stands for the ordinary gamma function (here, of $D/2$). Note that, for an integer valued D, Eq. (2.42) reproduces the familiar results such as $S(D=3) = 4\pi$, $S(D=2) = 2\pi$, and $S(D=1) = 2$. However, the above equation for $S(D)$, as well as our other discussions here, remain well defined even for noninteger D. The current I in Eq. (2.40) is, by Eq. (2.1), the flux of the surface current density $\vec{J}$ through the cluster base boundary being the surface of D-dimensional sphere with the radius $= R$. By Eq. (2.12) with $\partial h/\partial t \approx 0$, one has

$$-\vec{\nabla} \cdot \vec{J} = \Gamma\Omega\nabla^2 P = 0,$$

outside of the slowly evolving (quasistatic) clusters. In this dry region, $h \approx h_{\min}$. Therefore, in the equations of this section (as well as of the related Sec. V) we approximate $\Gamma(h)$ with the constant $\Gamma = \Gamma(h_{\min}) \approx \mu_{\text{sub}} h_{\min} = \mu_{\text{sub}} \Omega n_{\min} = D_{\text{sub}} \Omega n_{\min}/k_B T$; see Eq. (2.13b). Assuming here a radially symmetric solution, we obtain

$$J(r) = \frac{I}{S(D) r^{D-1}} = -\Gamma\Omega \frac{dP}{dr}, \quad \frac{dI}{dr} = 0, \tag{2.43}$$

outside of a slowly evolving (quasistatic) cluster, that is, for r in the range $R < r < \lambda$.

Here, λ is a characteristic distance corresponding to intercluster separation in Fig. 2 [35]. By integrating Eq. (2.43) over r in the range $R < r < \lambda$,

$$P(R) - P(\lambda) = \frac{F_D(\lambda, R)}{S(D)\Gamma\Omega} I. \tag{2.44}$$

Here, $F_D(\lambda, R) = \int_R^\lambda dr/r^{D-1}$, and thus

$$F_D(\lambda, R) = \frac{\lambda^{2-D} - R^{2-D}}{2-D}, \tag{2.45}$$

for $D \neq 2$, whereas for $D = 2$ we have,

$$F_{D=2}(\lambda, R) = \ln\left(\frac{\lambda}{R}\right). \tag{2.46}$$

Equation (2.44) can be solved for the current I,

$$I = S(D)\Gamma\Omega \frac{P(R) - P(\lambda)}{F_D(\lambda, R)}. \tag{2.44$'$}$$

The clusters are polydisperse in size, with smaller than average clusters [with, by Eq. (2.39), higher pressure] decaying by expelling their material into larger clusters [with, by Eq. (2.39), lower pressure]; see Fig. 2 (a). This coarsening yields a steady increase of average cluster height $H(t)$ and cluster base radius $R(t)$. The coarsening cluster growth is governed by the decay of the clusters that are comparable yet smaller than the average cluster size. For such a cluster $P_{\text{cluster}} \approx P(R) > P(\lambda) =$ the pressure of the nearest-neighbor (average size) cluster; see Fig. 2(a). Thus, by Eq. (2.44$'$), we have the scaling

$$I \sim S(D)\Gamma\Omega \frac{P_{\text{cluster}}}{F_D(\lambda, R)}. \tag{2.47}$$

In the Young-Laplace limit, the result in Eq. (2.39) applies. With it, Eq. (2.47) yields

$$I \sim \frac{\kappa m_Y}{R F_D(\lambda, R)}, \tag{2.47$'$}$$

with $\kappa = \Gamma\Omega\gamma$.

We note that the volume conservation law in Eq. (2.1) ensures that $V_{\text{cluster}} =$ the film volume initially (at $t = 0$) covering the base area $\sim \lambda^D$, i.e., by Eq. (2.41),

$$H R^D \sim h_0 \lambda^D, \tag{2.48}$$

with h_0, the initial film thickness. By Eqs. (2.38) and (2.48),

$$\lambda \sim (m_Y/h_0)^{1/D} R^{1+1/D}. \tag{2.49}$$

Note that by Eq. (2.49)

$$\frac{\lambda}{R} \sim \left(\frac{m_Y R}{h_0}\right)^{1/D} \sim \left(\frac{H}{h_0}\right)^{1/D} \gg 1, \tag{2.49$'$}$$

for large clusters with $H \gg h_0$.

The differential equation (2.40), in combination with Eqs. (2.38), (2.41), (2.47$'$), and (2.49), can be easily integrated to find the time scale of the cluster decay, with the result

$$t \sim R^{D+2} F_D(\lambda, R)/\kappa. \tag{2.50}$$

The cluster decay time scale $\sim$ evolution time [9], so Eqs. (2.49) and (2.50) directly yield the desired coarsening laws for the growth of $R, H \sim m_Y R$, and $\lambda \sim R^{1+1/D}$.

Case $D > 2$. As $\lambda \gg R$, for $D > 2$ one has, by Eq. (2.45), $F_D(\lambda, R) \sim R^{2-D}$. So, for $t \to \infty$, by Eqs. (2.50) and (2.38) one has

$$H/m_Y \sim R \sim (\kappa t)^{1/4} \tag{2.51}$$

for *any* $D > 2$.

Case $D = 2$. For this case, $F_{D=2}(\lambda, R) = \ln(\lambda/R)$, so for $t \to \infty$, Eqs. (2.49$'$) and (2.50) yield

$$t \sim R^4 \ln(R/R_0)/\kappa, \tag{2.52}$$

with $R_0 \sim h_0/m_Y$. By iteratively solving Eq. (2.52) for $R(t)$, we obtain

$$H/m_Y \sim R \sim [\ln(t/t_0)]^{-1/4}(\kappa t)^{1/4}, \tag{2.53}$$

with $t_0 \sim R_0^4/\kappa$, for $D = 2$ and $t \to \infty$. Thus, up to a very slowly varying logarithmic prefactor, one has $H \sim R \sim t^{1/4}$ for $t \to \infty$, in accord with our $D = 2$ simulations (discussed in Sec. III) and the experiments [13,15].

Case D < 2. As $\lambda \gg R$, for $D < 2$ one has, by Eqs. (2.45) and (2.49), $F_D(\lambda,R) \sim \lambda^{2-D} \sim [(m_Y/h_0)^{1/D} R^{1+1/D}]^{2-D}$, so by Eq. (2.50),

$$t \sim m_Y^{(2-D)/D} R^{(2+3D)/D} h_0^{-(2-D)/D}/\kappa. \tag{2.54}$$

By Eq. (2.54), for $D < 2$,

$$H/m_Y \sim R \sim t^{D/(2+3D)} \tag{2.55}$$

for $t \to \infty$. For $D = 1$, Eq. (2.55) yields

$$H/m_Y \sim R \sim t^{1/5} \text{ for } t \to \infty. \tag{2.56}$$

Let us summarize and discuss the above scaling behaviors. At long times, i.e., in the Young-Laplace limit, the cluster height $H \sim t^{1/4}$, for *any* $D \geqslant 2$ (a superuniversal behavior), in accord with the experiments [13,15], whence $D = 2$. In $D = 2$, however, in addition to the power law, there is also a slowly changing logarithmic correction displayed in Eq. (2.53). On the other hand, for $D < 2$, the superuniversality breaks down; $H \sim t^{\beta_H}$, with a D-dependent exponent $\beta_H = D/(2 + 3D)$. These scaling laws hold at *long times*, and they are insensitive to the actual form of the dewetting potential such the value of the exponent ω in Eq. (2.4). It is interesting to note that the result in our Eq. (2.56) for the special case $D = 1$ coincides with the result obtained for a *different* model in Ref. [30]. The model in Ref. [30] actually describes coarsening of *liquid* films, in which case the transport coefficient Γ depends on the interface height in a profound way, as $\Gamma(h) \sim h^3$, rather than being nearly constant as in the Mullins model for *solid* thin films discussed in Sec. II A. The existence of the logarithmic correction in $D = 2$ has also been noted in Ref. [31], for the case of liquid films coarsening. We also note that the above discussed breakdown of superuniversality was noted before in Ref. [31], for the case of liquid films. However, it has *not* been noted before that this breakdown of superuniversality occurs *only for* $D < 2$, as exhibited by our discussions above showing that $H \sim t^{1/4}$ for any $D \geqslant 2$.

Much like in our generalized Mullins model, in the models for liquid films [30–32], the mass transfer between clusters goes on over the dry areas with $h \approx h_{\min}$. Thus, the formal replacement $\Gamma(h) \to \Gamma(h_{\min})$ will not affect much the cluster coarsening dynamics *if* the diffusive intercluster mass transfer is the dominant coarsening mechanism. With this replacement, the liquid film models become identical to the generalized Mullins model with an h-independent transport coefficient $\Gamma(h) = \Gamma(h_{\min})$. However, the mass transfer is not the only possible coarsening mechanism. The clusters growth may also go by their fusion (coalescence). This mechanism is effective only if clusters can migrate during their lifetimes [given by Eq. (2.52) for $D = 2$] by a distance λ_{life} which is comparable or larger than the typical intercluster distance λ in Eq. (2.49). The cluster migration has been discussed in detail in Ref. [32] for a generic $\Gamma(h) \sim h^q$. In general, the details of cluster migration were found to be strongly dependent on the value of the exponent q [32]. Note that the formal limit $q \to 0$ corresponds to the generalized Mullins model Eq. (2.12) with an h-independent transport coefficient. The results of Ref. [32] can be used to estimate the ratio $\lambda_{\text{life}}/\lambda$, which turns out to crucially depend on the initial film thickness h_0. By applying the results of Ref. [32] to initially very thin (atomically thin) films with $h_0 \sim h_{\min} \sim$ atomic size, one finds that, for $q \leqslant 3$, the ratio $\lambda_{\text{life}}/\lambda \sim 1$ only for microscopically (atomically) small clusters, and, as these clusters grow in time, $\lambda_{\text{life}}/\lambda \to 0$ for $t \to \infty$. Thus, quite generally (for both solid and liquid clusters), cluster coalescence plays a subdominant role relative to the mass transfer *if* the initial film is atomically thin, i.e., $h_0 \sim h_{\min}$. With such an initial condition, the liquid film models will yield nearly the same coarsening behavior as generalized Mullins model, which is dominated by intercluster mass transfer mechanism. The condition $h_0 \sim h_{\min}$ is indeed assumed in the Sec. III simulations of the generalized Mullins model; see Sec. II D discussions. Under this condition, our results in Secs. III, IV, and V can also be used to discuss the experimental systems with liquid clusters. We stress again that this assertion is applicable (at least) to the systems with initially very thin films with $h_0 \sim h_{\min}$. Experimentally, this condition corresponds to very thin films, obtained by depositing a few monolayers or a submonolayer. In fact, the films of the significant experimental studies [13] and [15] are indeed formed with such depositions. The authors of Ref. [13] have actually claimed the absence of (liquid) cluster coalescence in their experiments. This is in accord with the above discussion. In our $D = 2$ simulations of the generalized Mullins model with $h_0 \sim h_{\min}$ (Sec. III), we also did not see some significant cluster coalescence. Some migration of cluster centers was seen [see our Fig. 3], but it was never large enough to bring two clusters into coalescence during their lifetimes. This is in accord with the above analytic conclusion that $\lambda_{\text{life}}/\lambda \ll 1$ for initially very thin (atomically thin) films with $h_0 \sim h_{\min} \sim$ atomic size.

A more quantitative support for these claims is provided in Sec. V, in which we develop an analytic theory to calculate the effective, cluster-size-dependent coarsening exponents [such as the one in Eq. (1.3)]. The theory takes into account only intercluster mass transfer mechanism and ignores cluster coalescence. In Sec. V, the theory's results are compared with our Sec. III simulations (done with $h_0 \sim h_{\min}$, see Sec. II D) and a very good agreement is found. The agreement of this (coalescence free) theory with the simulations shows that the coalescence does not play substantial role in very thin films with $h_0 \sim h_{\min}$. See the figures displayed in Sec. V. Some differences between the theory and the simulations seen at the earliest times may be attributed to the coalescence of very small clusters. However, as the clusters grow and become well separated, the coalescence becomes insignificant. Thus, the dominant coarsening mechanism becomes the coarsening via diffusive mass transfer over the dry area where $h(\vec{x},t) \approx h_{\min}$.

Overall, the coarsening dynamics of initially very thin liquid films can effectively be described by the generalized Mullins model with constant transport coefficient $\Gamma(h_{\min})$. In view of this, our results in Secs. III, IV, and V can also be used to discuss the experimental systems with liquid clusters. We stress again that this assertion is applicable to the

systems with initially very thin films with a few monolayers, as in the experiments of Refs. [13]. This is documented by our simulations of the generalized Mullins model (Sec. III), which do indeed exhibit the same major features of the effective coarsening exponents of the liquid clusters seen in the experiments of Ref. [13]. On the other hand, for initially thick films (with many monolayers), cluster coalescence will become significant, and we anticipate significant differences between solid and liquid films coarsening behaviors. The ultimate (infinite time) coarsening behavior will still be the same (with cluster height $\sim t^{1/4}$ for $D = 2$), yet cluster coalescence may produce significant crossover behaviors that are different for solid and liquid films which are initially thick ($h_0 \gg h_{\min} \sim$ atomic size).

For the future purposes of Secs. IV and V, it is convenient to express the quasistatic cluster pressure P, height H, and base radius R as functions of the cluster volume V. This can easily be done in the Young-Laplace limit, by a straightforward application of Eqs. (2.36), (2.38), (2.39), and (2.41), yielding

$$H_{\rm stat}^{\rm Young}(V) = C_H V^{1/3}, \quad R_{\rm stat}^{\rm Young}(V) = C_R V^{1/3}, \quad P_{\rm stat}^{\rm Young}(V) = C_P V^{-1/3}, \tag{2.57}$$

for the physically interesting case $D = 2$. In Eq. (2.57),

$$C_H = (2\pi)^{-1/3} m_Y^{2/3}, \quad C_R = (4/\pi)^{1/3} m_Y^{-1/3}, \quad C_P = \gamma (2\pi)^{1/3} m_Y^{4/3}. \tag{2.58}$$

For example, for our rescaled model of Sec. II D, with $\gamma = 1$, by Eqs. (2.58) and (2.34),

$$C_H = (2\pi)^{-1/3} \left(\frac{2(2\omega+1)}{\omega(\omega+2)}\right)^{1/3}, \quad C_R = (4/\pi)^{1/3} \left(\frac{2(2\omega+1)}{\omega(\omega+2)}\right)^{-1/6}, \quad C_P = (2\pi)^{1/3} \left(\frac{2(2\omega+1)}{\omega(\omega+2)}\right)^{2/3}. \tag{2.59}$$

III. CLUSTER COARSENING GROWTH: RESULTS FROM NUMERICAL SIMULATIONS

A. Statistical quantities characterizing clusters

This section describes quantitative results of our simulations of the interface dynamics of the rescaled model defined in Sec. II D; see Eqs. (2.23)–(2.25) and (2.32) and Sec. II D for our numerical procedure description. In this model, we consider the dewetting potentials with $\omega = 1, \omega = 2$, and $\omega = 6$ in Eq. (2.24). In this and the following sections, we focus on the physically interesting case with $D = 2$; see Fig. 4 from our simulations. After an initial stage characterized by formation of pits, the interface eventually structures as an ensemble of clusters that grow via a coarsening process. As seen in Fig. 4, the clusters are polydisperse in sizes, with smaller than average clusters decaying by expelling their material into larger clusters (recall the Sec. II E discussion): Compare, for example, the cluster ensembles seen in the last two panels of Fig. 4(b). Due to the decay of the small clusters, the total number of clusters $N(t)$ in the system decreases in time while the average cluster volume $\langle V \rangle$ increases in time; see Fig. 5. This coarsening yields a steady growth of the average cluster height and cluster base radius; see Fig. 4. In the following, we introduce basic statistical quantities that we used to characterize the evolving ensemble of growing clusters exemplified in Fig. 4 from our simulations. By using interface configurations such those seen in Fig. 4, we counted clusters to obtain their number $N(t)$ in the simulation sample at time t. We measured the heights of individual clusters, H_n [$n = 1$,

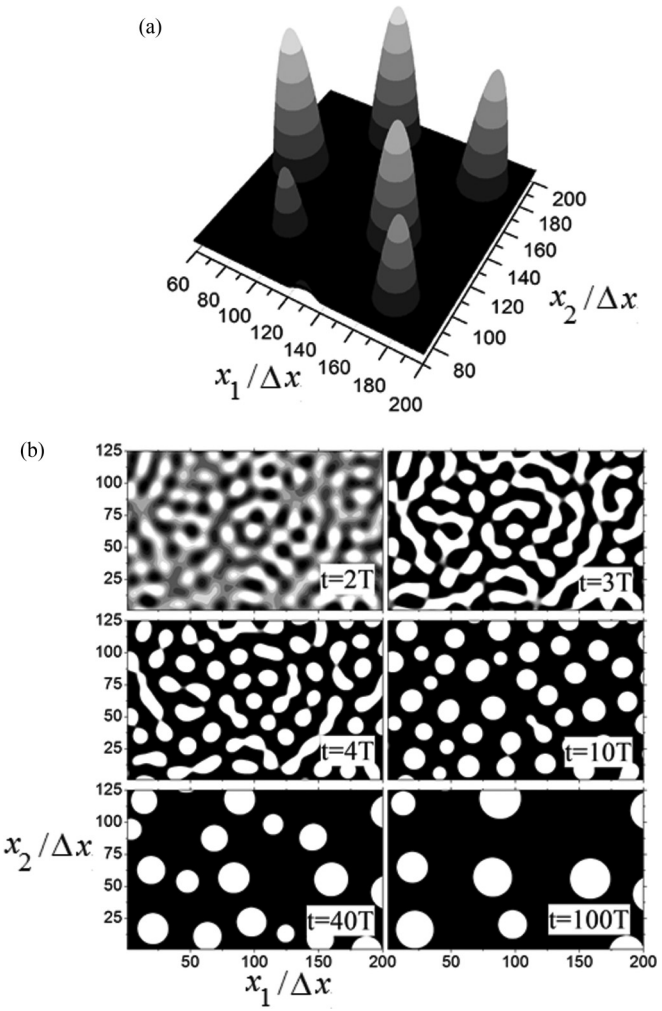

FIG. 4. Panel (a) exhibits the ultimate stage of the $D = 2$ thin film interface evolution, dominated by the presence of growing clusters. Panel (b) exhibits interface height contour plots showing film morphology evolution for $D = 2$ and $\omega = 1$, from the simulation of the rescaled model with dimensionless $t, \vec{x}, h$ (Sec. II D). Here, as in Fig. 3, $T = 39.0625 = 10^4\ \Delta t$. Note the emergence of the transient wormlike morphology seen at $t \approx 3T$. For $t < 3T$, the interface is in a time stage characterized by pit formation [as in Fig. 2(b)]. For $t > 3T$, the interface is characterized by the formation of slowly growing clusters [as in panel (a) here]. We note that in the above panels we depict only a smaller portion (about 4%) of the simulated system which actually contains about thousand clusters at $t \sim 10T$. We also note that for each dewetting potential (i.e., each ω) we simulated ten samples and the statistical data displayed in the following figures are obtained by taking the average of the data obtained from the samples.

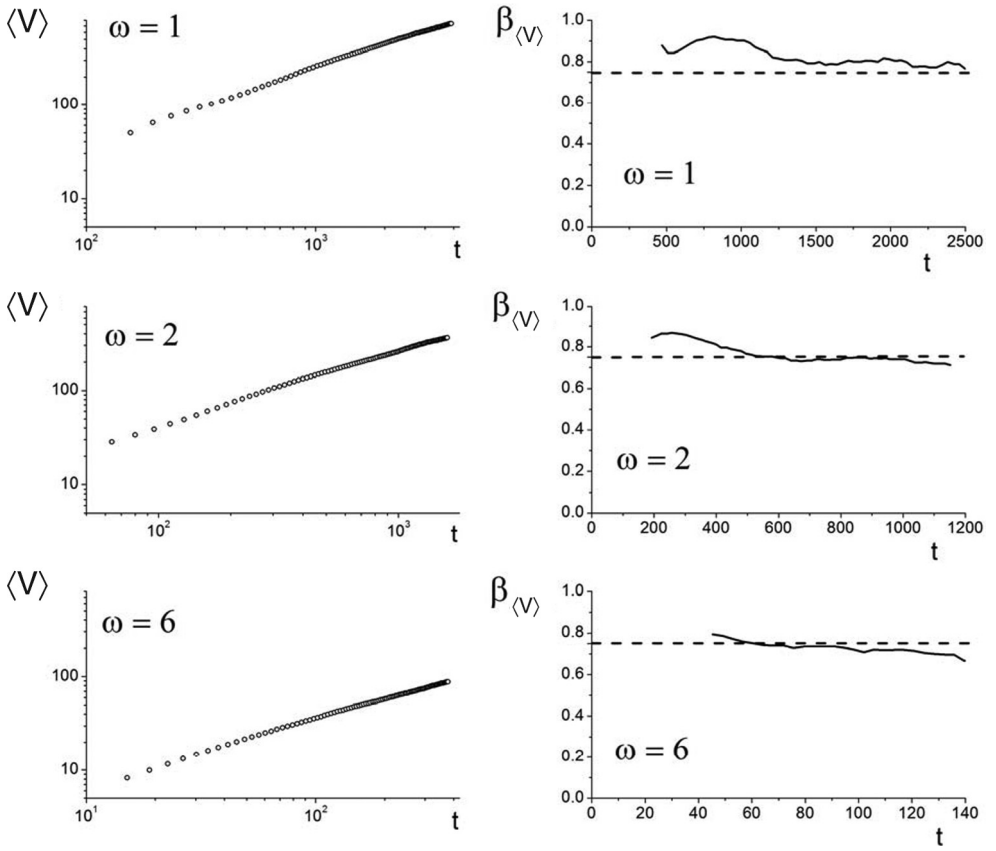

FIG. 5. Temporal evolution of the clusters average volume $\langle V\rangle$ in the systems we simulated, with ω= 1,2, and 6. We also present the evolution of the corresponding effective coarsening exponent, $\beta_{\langle V\rangle}(t) = d\ \ln[\langle V\rangle]/d\ \ln(t)$. This exponent is expected to approach the value of $+3/4$ (dashed line) at long times. There are, however, significant deviations away from this value, which are seen in the $\beta_{\langle V\rangle}(t)$ at early times.

2, 3, . . . , $N(t)$], to obtain the average cluster height,

$$\langle H\rangle = \frac{\sum_{n=1}^{N(t)} H_n}{N(t)}. \tag{3.1}$$

[See the remark after Eq. (3.10) in the following.] We also measured the pressure at the center of each cluster, P_n, to obtain the average cluster pressure,

$$\langle P\rangle = \frac{\sum_{n=1}^{N(t)} P_n}{N(t)}. \tag{3.2}$$

Another important quantity characterizing our film is the size of the wet area, i.e., the area covered by clusters (the "white area" in Fig. 4). To extract it, we used a convention involving a characteristic height scale h^*, below which the interface height approaches its asymptotic value $\approx h_{\min}$ [see Sec. IV and Fig. 9(b) therein]. Thus, the interface sections with $h(\vec{x},t) < h^*$ can be identified as dry areas, whereas, the interface sections with $h(\vec{x},t) > h^*$ can be identified as wet areas, i.e., clusters. The total wet area is thus given by the surface integral,

$$A_{\rm wet}(t) = \iint_{\rm wet} d^2\vec{x} = \iint_{\rm sample} d^2\vec{x}\,\theta(h(\vec{x},t) - h^*). \tag{3.3}$$

Here, $\theta(z)$ is the usual step function [$\theta(z) = 1$ for $z > 0$ and $\theta(z) = 0$ for $z < 0$]. The total wet area Eq. (3.3) is obviously smaller than the entire substrate area,

$$A_{\rm sample} = \iint_{\rm sample} d^2\vec{x}. \tag{3.4}$$

The area fraction occupied by clusters ("wet area fraction") is thus

$$\phi(t) = \frac{A_{\rm wet}(t)}{A_{\rm sample}} = \frac{\iint_{\rm wet} d^2\vec{x}}{\iint_{\rm sample} d^2\vec{x}} = \frac{\iint_{\rm sample} d^2\vec{x}\,\theta(h(\vec{x},t) - h^*)}{\iint_{\rm sample} d^2\vec{x}}. \tag{3.5}$$

We stress that the above employed height scale h^* is not a sharply defined quantity. One possible choice would be to identify h^* with the inflection point of the dewetting potential $\Phi_{\rm eff}(h)$, i.e., $\Phi_{\rm eff}{}''(h^*) = 0$. We have, however decided for a different convention defining the h^* via the condition that the third derivative of $\Phi_{\rm eff}(h)$ vanishes at h^*. For the here interesting rescaled model potential in Eqs. (2.24) and (2.25), this condition gives $h^* = 1$ for any ω, as discussed in Sec. II D.

The base areas of the clusters are nonoverlapping (see Fig. 4), so the total wet area is simply the sum of all clusters base areas,

$$A_{\rm wet}(t) = \sum_{n=1}^{N(t)} A_n. \tag{3.6}$$

Thus, by Eqs. (3.6) and (3.3), the average cluster base area is

$$\langle A\rangle = \frac{\sum_{n=1}^{N(t)} A_n}{N(t)} = \frac{\iint_{\text{sample}} d^2\vec{x}\theta(h(\vec{x},t)-h^*)}{N(t)}. \quad (3.7)$$

We also measured the base area of each individual cluster, A_n $[n = 1, 2, 3, \ldots, N(t)]$. Cluster bases are nearly circular (see Fig. 4 from our simulations), so one can introduce the base radius of the nth cluster via

$$\pi R_n^2(t) = A_n \Rightarrow R_n = \sqrt{\frac{A_n}{\pi}}. \quad (3.8)$$

Using (3.8), we calculated the average cluster base radius via

$$\langle R\rangle = \frac{\sum_{n=1}^{N(t)} R_n}{N(t)}. \quad (3.9)$$

Another quantity of interest is the total volume of the film inside clusters, i.e., the volume of the film covering wet areas with $h(\vec{x},t) > h^*$. Away from the clusters $\tilde{h}(\vec{x},t) \approx h_{\min}$ so the actual film volume part which is within the clusters is essentially above $h_{\min}$ and it is best described by introducing the reduced height,

$$\tilde{h}(\vec{x},t) = h(\vec{x},t) - h_{\min}. \quad (3.10)$$

Thus, for example, the nth cluster height H_n is defined by Eq. (3.10) with $\vec{x}$ being the center of the cluster base area. The total film volume above the $h_{\min}$ level covering all wet areas $[h(\vec{x},t) > h^*]$ is

$$\iint_{\text{wet}} d^2\vec{x}\tilde{h}(\vec{x},t) = \iint_{\text{sample}} d^2\vec{x}\theta(h(\vec{x},t)-h^*) \cdot [h(\vec{x},t)-h_{\min}]. \quad (3.11)$$

This volume is the sum of volumes of individual clusters, V_n $[n = 1, 2, 3, \ldots, N(t)]$, so,

$$\sum_{n=1}^{N(t)} V_n = \iint_{\text{sample}} d^2\vec{x}\theta(h(\vec{x},t)-h^*)\cdot[h(\vec{x},t)-h_{\min}]. \quad (3.12)$$

Thus, the average volume of a cluster is given by

$$\langle V\rangle = \frac{\sum_{n=1}^{N(t)} V_n}{N(t)} = \frac{\iint_{\text{sample}} d^2\vec{x}\theta(h(\vec{x},t)-h^*)\cdot[h(\vec{x},t)-h_{\min}]}{N(t)}. \quad (3.13)$$

In the following, we discuss the dynamics of the numerous statistical quantities introduced in this section by using the results obtained from our simulations for three different values of ω ($\omega = 1$, 2, and 6). To suppress statistical fluctuations, all statistical quantities are obtained by taking the average of data obtained from ten statistically independent simulations (samples) done for each studied value of ω.

B. Dynamics of cluster sizes and pressure: Time-dependent coarsening exponents

In Figs. 5 through 7, we display our simulation results for the time evolution of the four basic statistical quantities characterizing cluster ensemble: average cluster volume $\langle V\rangle$, average cluster pressure $\langle P\rangle$, average cluster height $\langle H\rangle$, and average cluster radius $\langle R\rangle$. These quantities are extracted from our simulation results, using their definitions in Eqs. (3.1), (3.2), (3.9), and (3.13). In Figs. 5 through 7, we also display the evolution of the effective coarsening exponents, defined by

$$\beta_{\langle V\rangle}(t) = \frac{d\ln(\langle V\rangle)}{d\ln(t)}, \quad \beta_{\langle P\rangle}(t) = \frac{d\ln(\langle P\rangle)}{d\ln(t)}, \quad \beta_{\langle H\rangle}(t) = \frac{d\ln(\langle H\rangle)}{d\ln(t)}, \quad \beta_{\langle R\rangle}(t) = \frac{d\ln(\langle R\rangle)}{d\ln(t)}. \quad (3.14)$$

We used the methodology of Amar *et al.* [36] to numerically calculate these effective exponents from our simulation data for $\langle V\rangle$, $\langle P\rangle$, $\langle H\rangle$, and $\langle R\rangle$. From Figs. 5 through 7, we see that these effective exponents significantly depend on time t. The exponents seen in these figures deviate from the asymptotic values expected at long times on the basis of the Young-Laplace model for clusters (Sec. II E). By the Sec. II E discussions (for $D = 2$), these asymptotic exponents are given by

$$\beta_{\langle H\rangle}(t=\infty) = \beta_{\langle R\rangle}(t=\infty) = \tfrac{1}{4} \quad (3.15)$$

and by Eq. (2.41),

$$\beta_{\langle V\rangle}(t=\infty) = \beta_{\langle H\rangle}(t=\infty) + 2\beta_{\langle R\rangle}(t=\infty) = \tfrac{3}{4}, \quad (3.16)$$

while, by Eq. (2.39),

$$\beta_{\langle P\rangle}(t=\infty) = -\beta_{\langle H\rangle}(t=\infty) = -\tfrac{1}{4}. \quad (3.17)$$

The above asymptotic (Young-Laplace) coarsening exponents are universal; i.e., they do not depend on the dewetting potential details such as the value of ω in Eq. (2.4). However, the simulation results displayed in Figs. 5 through 7 do evidence significant early time departures away from the above universal long time coarsening exponents. Moreover, the simulation results indicate that these departures are correlated with the long range character of the potential. For example, from Fig. 6, for a large $\omega = 6$ (essentially, a short range dewetting potential), the early time range cluster height exponent $\beta_{\langle H\rangle}$ is about 0.28, so it is close to the universal asymptotic $\beta_{\langle H\rangle} = 0.25$. On the other hand, by Fig. 6, for genuine long-range potentials with for $\omega = 1$ and $\omega = 2$, the early time range exponent $\beta_{\langle H\rangle}$ is about 0.33; i.e., it significantly deviates from the asymptotic $\beta_{\langle H\rangle} = 0.25$. It is of direct physical interest to understand these effects. Indeed, the potentials $\omega = 1$ and $\omega = 2$ are physically interesting, as discussed in Sec. I. In addition, as noted in the Introduction (Sec. I), an effective (early time) exponent for the growth of cluster height, estimated to be $\beta_H^{\text{eff}} \approx 0.33$, has been indeed observed in experiments [13]. In view of the above discussion, by the results of our simulations in Fig. 5, we suggest that the experimentally seen (in Ref. [13]) early time coarsening exponent emerges as an effect of the long-range dewetting interactions such as the van der Waals potential Eq. (1.1), corresponding to the case $\omega = 2$.

The above simulation results show that the deviations from the predictions of the Young-Laplace model are larger for smaller values of ω, i.e., for longer ranged dewetting

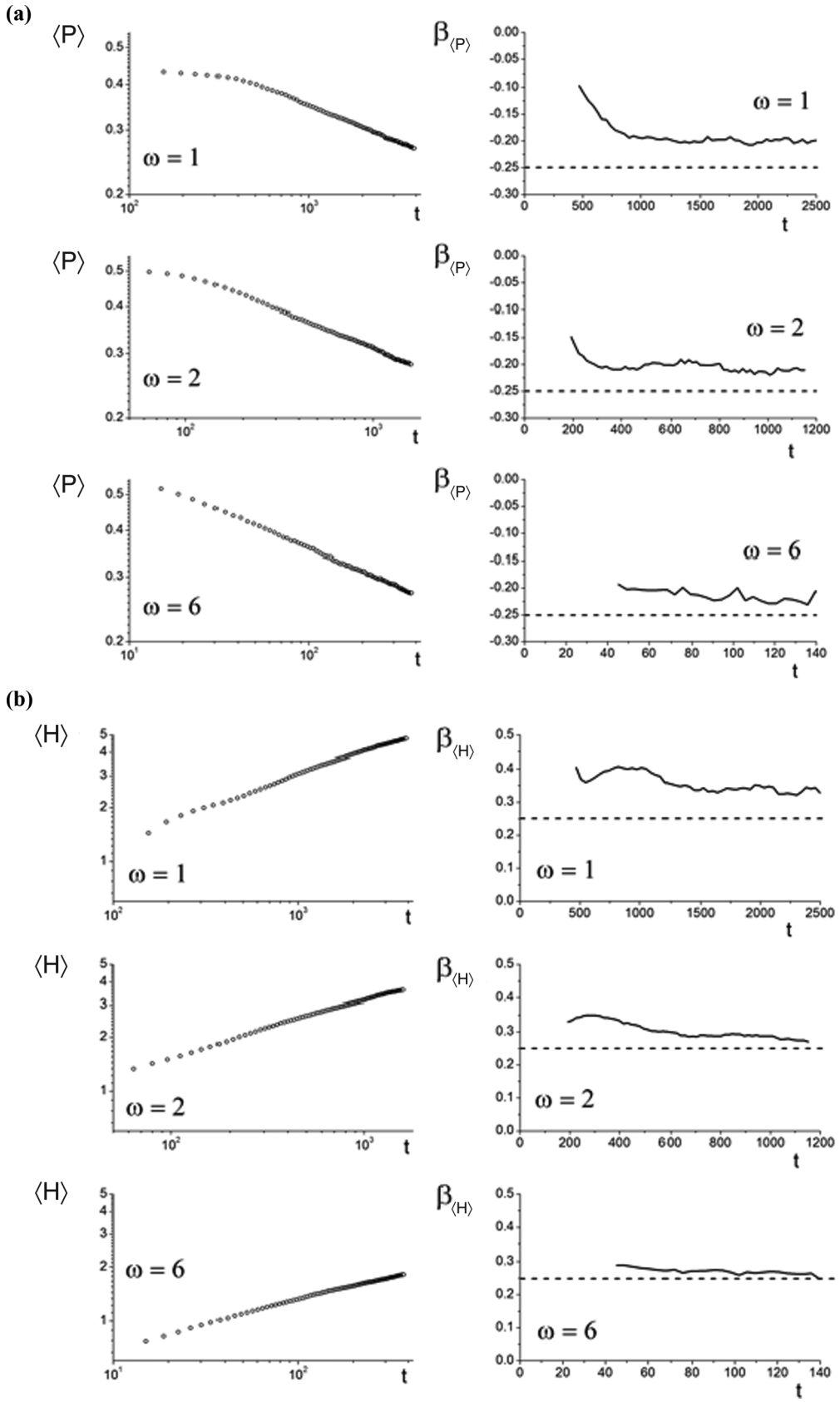

FIG. 6. Evolution of the clusters average pressure $\langle P\rangle$, in (a) and cluster average height $\langle H\rangle$, in (b), in the systems with $\omega = 1$, 2, and 6. Also given are the effective coarsening exponents, $\beta_{\langle P\rangle}(t) = d\ \ln[\langle P\rangle]/d\ \ln(t)$ (expected to approach $-1/4$ at long times), and $\beta_{\langle H\rangle}(t) = d\ \ln[\langle H\rangle]/d\ \ln(t)$ (expected to approach $+1/4$ at long times). There are, however, significant deviations away from these asymptotic values that are seen at early times.

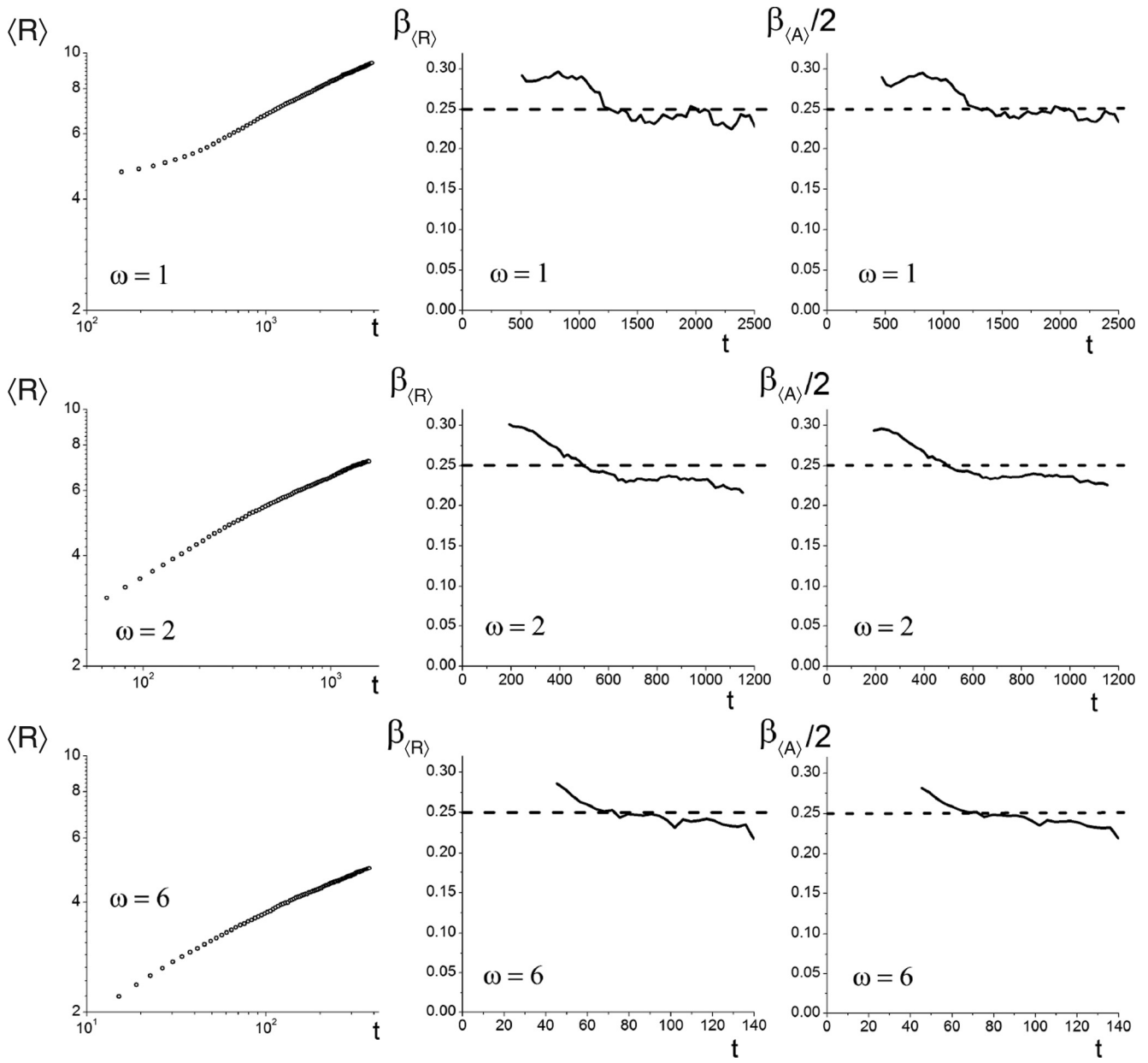

FIG. 7. Time evolution of the clusters average base radius $\langle R\rangle$ in the systems we simulated with $\omega = 1,2$, and 6. We also display the corresponding effective exponent, $\beta_{\langle R\rangle}(t) = d\ \ln[\langle R\rangle]/d\ \ln(t)$ vs time. This exponent expected to approach the value of $+1/4$ at long times. There are, however, significant deviations away from this value, which are seen in the $\beta_{\langle R\rangle}(t)$ at early times. For comparison, we also display $\beta_{\langle A\rangle}(t)/2$, where $\beta_{\langle A\rangle}(t) = d\ \ln[\langle A\rangle]/d\ \ln(t)$ is the effective exponent for the growth of cluster base area.

interactions. To illustrate this point, in Fig. 8 we plot the time evolution of the quantity

$$\frac{\frac{2\langle H\rangle}{\langle R\rangle}}{m_Y}. \tag{3.18}$$

By Eq. (2.46), we have for the nth cluster (in the Young-Laplace limit)

$$2H_n = m_Y R_n \Rightarrow 2\langle H\rangle = m_Y\langle R\rangle. \tag{3.19}$$

Thus, the quantity in Eq. (3.18) is exactly *1* in the Young-Laplace limit. However, from our simulation results in Fig. 8 (bottom panel) we see that the aspect ratio $2\langle H\rangle/\langle R\rangle$ is, at early times, significantly smaller than the Young angle slope m_Y, especially for the smaller values of ω, i.e., for longer range dewetting interactions. As documented in Fig. 8 (top panel), this effect is correlated with the magnitude of the departures of the effective coarsening exponents from their asymptotic values, which are larger for smaller values of ω, i.e., for the longer range interactions with $\omega = 1$ or 2.

This breakdown of the classical Young-Laplace model will be discussed analytically in the Sec. IV as well as in Sec. V, in which we develop a cluster coarsening dynamics theory capable of calculating the effective coarsening exponents and analytically explain the results of this section simulations.

Our analytic theory is used in Sec. V F to explain another interesting feature seen in the simulations: The exponents $\beta_{\langle H\rangle}$,

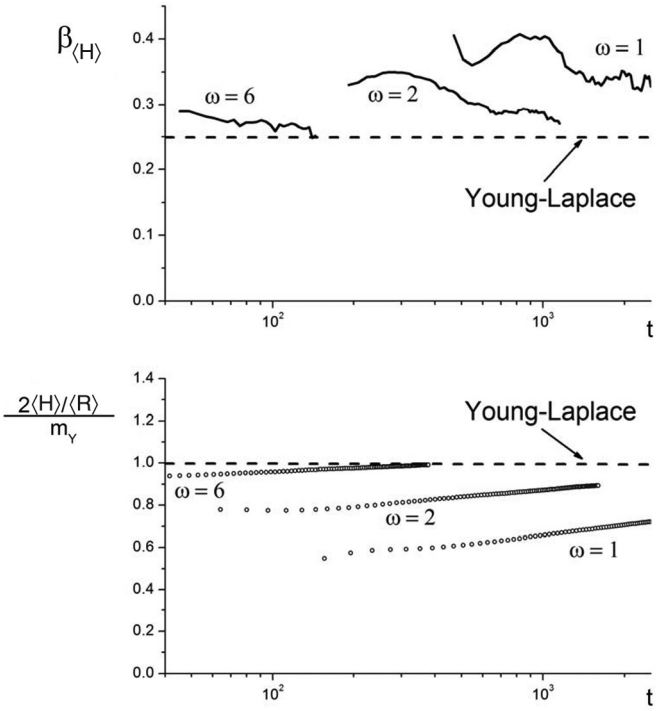

FIG. 8. The figure qualitatively documents the correlation between the failure of the Young-Laplace model prediction for cluster aspect ratio (bottom panel), with the magnitude of the deviations of the effective exponent $\beta_{\langle H\rangle}$ away from its asymptotic value (top panel). Both effects increase with decreasing ω.

$\beta_{\langle R\rangle}$, and $\beta_{\langle V\rangle}$ approach their asymptotic values in Eqs. (3.15) and (3.16) in a *nonmonotonous* fashion by first crossing their asymptotic values (from above) at a *finite* characteristic time. This time is different for different coarsening exponents: For $\beta_{\langle V\rangle}$ the crossing time is shorter than our simulation time for $\omega = 2$ and 6, whereas it is longer for $\omega = 1$ (see Fig. 5); for $\beta_{\langle H\rangle}$ all crossing times are actually longer than our available simulation times [see Fig. 6(b)]; for $\beta_{\langle R\rangle}$ the crossing times are all shorter than our simulation times (see Fig. 7). The analytic theory presented in Sec. V F reproduces this finite time crossing of the asymptotic values for these effective exponents. See Fig. 15 and the discussions at the end of Sec. V F explaining the competing effects producing the crossing phenomenon. On the other side, as inferred from Fig. 6(a) from our simulations, there is no such finite time crossing for the pressure exponent $\beta_{\langle P\rangle}$. This will be independently confirmed by our analytic theory results for $\beta_{\langle P\rangle}$ presented in Sec. V F; see Fig. 15 therein, which indeed shows that this exponent does not cross its asymptotic value at any finite time.

Finally, also interesting is the scaling of the average cluster base area Eq. (3.7). The associated effective coarsening exponent is

$$\beta_{\langle A\rangle}(t) = \frac{d\ln(\langle A\rangle)}{d\ln(t)}. \tag{3.20}$$

Crudely, $\langle A\rangle$ is approximately $\pi\langle R\rangle^2$, so one may expect,

$$\beta_{\langle A\rangle}(t) \approx 2\beta_{\langle R\rangle}(t) \Rightarrow \frac{\beta_{\langle A\rangle}(t)}{2} = \beta_{\langle R\rangle}(t), \tag{3.21}$$

at any t, and, in particular,

$$\beta_{\langle A\rangle}(t=\infty) = 2\beta_{\langle R\rangle}(t=\infty) = \tfrac{1}{2}, \tag{3.22}$$

in the infinite time, Young-Laplace limit. To check the validity of the approximate relation (3.21), in Fig. 7 we plot our simulation results for both $\beta_{\langle A\rangle}/2$ and $\beta_{\langle R\rangle}$. The approximate character of Eq. (3.21) is evident from these plots.

IV. CLUSTERS MORPHOLOGY BEYOND THE CLASSICAL YOUNG-LAPLACE MODEL

A. Quasistatic clusters

In this and the following section (Sec. V), we develop an analytic theory aimed to explain the results of our Sec. III interface dynamics simulations of the cluster coarsening. Our main goal is to elucidate the effects of the long range dewetting interactions on the character of the cluster coarsening dynamics. Our simulations suggest that the long range dewetting interactions produce significant early time departures from the asymptotic predictions based on the classical Young-Laplace cluster model (Sec. II E). For example, within this model, the cluster height (H)-to-radius (R) aspect ratio does not depend on the cluster size. By Eq. (38) of Sec. II, in the Young-Laplace limit we have

$$\frac{2H}{R} \approx m_Y = \tan(\theta_Y), \tag{4.1}$$

indicating that the aspect ratio is a constant expressible in terms of the Young angle slope. Likewise, by the discussions of Sec. II E, in the Young-Laplace static cluster model for $D = 2$ we have the following simple results for cluster height, cluster base radius, and cluster pressure, expressed as functions of the cluster volume,

$$\begin{aligned} &H_{\rm stat}^{\rm Young}(V) = C_H V^{1/3}, \quad R_{\rm stat}^{\rm Young}(V) = C_R V^{1/3}, \\ &P_{\rm stat}^{\rm Young}(V) = C_P V^{-1/3}, \end{aligned} \tag{4.2}$$

with C_H, C_R, C_P being numerical constants expressible in terms of the Young angle slope; see Eqs. (2.57)–(2.59). However, the clusters seen in the simulations strongly deviate from Young-Laplace behavior in Eqs. (4.1) and (4.2). Moreover, in Sec. III, we have found that these deviations are larger for smaller values of ω, i.e., for longer ranged dewetting interactions. Recall, for example, of Fig. 8 of Sec. III, which shows that, in contrast to Eq. (4.1), the ratio $2H/R$ is, at early times, significantly smaller than the Young angle slope m_Y, especially for smaller values of ω, i.e., for longer ranged dewetting interactions. As documented in Fig. 8 of Sec. III, this effect is correlated with the magnitude of the departures of the coarsening exponents from their asymptotic values, which are larger for smaller values of ω such as $\omega = 1$ or 2, corresponding to the physically interesting dewetting interactions discussed in Sec. I.

To quantify these effects, in this section we pursue a mathematical discussion of quasistatic clusters shapes and sizes that goes beyond the Young-Laplace model. Our discussion will be used in the following section (Sec. V), to develop a powerful cluster dynamics theory capable of analytically explaining the findings of our simulations and related results from the experiments.

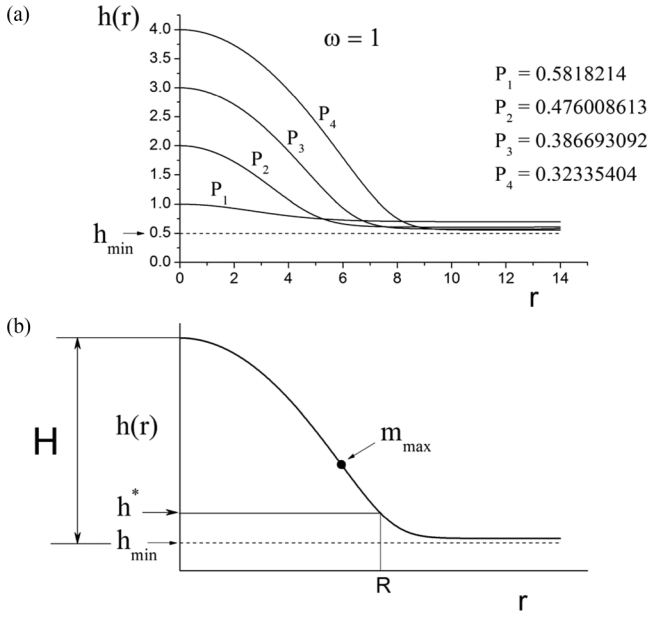

FIG. 9. (a) Cluster profiles obtained by solving Eq. (4.3) for $\omega = 1$ for several different pressures. To obtain the cluster type solutions, for each cluster height H, the pressure is fixed by the boundary condition that the interface height approaches a finite value at infinity. (b) The figure conceptualizes the definition of the cluster radius R. Also labeled is the inflection point of the cluster profile at which the interface slope reaches its maximum value $m_{\max}$.

Clusters occurring in our simulations are evolving very slowly and can be considered as (nearly) time-independent, static objects with (nearly) constant pressure. Thus, for $D = 2$, the radial profile of a single cluster can be described by Eq. (2.10) with $\gamma(h) = \gamma$,

$$\gamma\left[\frac{d^2h}{dr^2} + \frac{1}{r}\frac{dh}{dr}\right] - \Phi'_{\rm eff}(h) = -P_{\rm stat}, \tag{4.3}$$

with $P_{\rm stat}$ being the static cluster pressure [see also Eq. (A7) in Appendix A]. Here, we outline the results obtained by solving Eq. (4.3), for our rescaled model of Sec. II D, with $\gamma = 1$, and

$$\Phi'_{\rm eff}(h) = \frac{1}{h^{\omega+1}}\left[1 - \left(\frac{h_{\min}}{h}\right)^{\omega}\right], \tag{4.4}$$

where

$$h_{\min} = \left(\frac{\omega+2}{2(2\omega+1)}\right)^{1/\omega}. \tag{4.5}$$

For a given cluster height H [above the dry area, at $h = h_{\min}$; see Fig. 9(b)], we solved Eq. (4.3) numerically (using Wolfram's MATHEMATICA), with the boundary conditions

$$h(r=0) = H + h_{\min}, \left.\frac{dh}{dr}\right|_{r=0} = 0. \tag{4.6}$$

For any given H, the value of the cluster pressure $P_{\rm stat}$ in Eq. (4.3), is chosen such that the $h(r)$ approaches a *finite* value ($\approx h_{\min}$) in the limit of infinite r; see Fig. 9(a). Thus, by imposing this boundary condition at infinity, we are able to find the functional relation $P_{\rm stat}(H)$ expressing the cluster pressure $P_{\rm stat}$ as a function of the cluster height H. For the purposes of Sec. V, it will be, however, more convenient to express $P_{\rm stat}$ as a function of the cluster volume, defined in the same sense as in Sec. III A, as

$$V = 2\pi \int_0^R dr\, r[h(r) - h_{\min}]. \tag{4.7}$$

Here, R is the cluster base radius, fixed by the condition $h(r = R) = h^*$, with h^* being a characteristic height below which $h(r)$ exponentially approaches its asymptotic value (at infinite r); see Fig. 9(b). The h^* is not a sharply defined quantity. One possible choice would be to identify it as the inflection point of the dewetting potential $\Phi_{\rm eff}(h)$. We have, however, decided for a different convention defining the h^*, via the condition that the third derivative of $\Phi_{\rm eff}(h)$ vanishes at h^*. We recall that the same convention is used in Sec. III to define clusters from our simulations. For the rescaled model potential in Eq. (4.4), this convention gives $h^* = 1$ for any ω, as discussed in Sec. II D.

By the above described procedure, we have constructed the functional relations,

$$P_{\rm stat}(V), \quad H_{\rm stat}(V), \quad R_{\rm stat}(V), \tag{4.8}$$

expressing cluster pressure, cluster height, and cluster base radius, as functions of the cluster volume. Our numerical results for these functions are given in Fig. 10, for the rescaled models with $\omega = 1,2$, and 6. See also Sec. IV B in the following. In Fig. 10, for comparison, we also indicate the corresponding results for the Young-Laplace cluster model, Eq. (4.2). Evidently, the Young-Laplace model is correct only asymptotically (in the large-V limit), and there are significant departures away from it for the dewetting potentials with smaller values of ω such as $\omega = 1$ and $\omega = 2$.

In Fig. 11 we display several quantities further evidencing the magnitude of the breakdown of the Young-Laplace cluster model. Thus, in Fig. 11(a)), we display the quantity,

$$\frac{m_{\max}(H)}{m_Y}, \tag{4.9}$$

versus cluster height H. Here, $m_{\max} = |dh/dr|_{\max}$ is the maximum interface slope occurring at the inflection point of the cluster profile; see Fig. 9(b). The $m_{\max}$ approaches the Young angle slope m_Y for large H, so the ratio in Eq. (4.9) approaches *1* in the Young-Laplace limit. However, for a finite H, this ratio is smaller than one, and this effect is especially prominent for dewetting potentials with smaller values of ω such as $\omega = 1$ and $\omega = 2$. On the other side, for a large $\omega = 6$ (essentially, a short range potential), the ratio in Eq. (4.9) quickly approaches 1, i.e., the Young-Laplace limit. The same trend is seen in other quantities displayed in Fig. 11 for various values of ω. Thus, in Fig. 11(b) we display the ratio

$$\frac{\frac{2H}{R_{\rm stat}(H)}}{m_Y}, \tag{4.10}$$

which by Eq. (4.1) approaches *1* in the Young-Laplace limit of infinite cluster height H. We also display, in Fig. 11(c),

$$\frac{P_{\rm stat}(H)}{P_{\rm stat}^{\rm Young}(H)}, \tag{4.11}$$

being the ratio between the true pressure of a cluster with height H and the Young-Laplace model pressure for a cluster

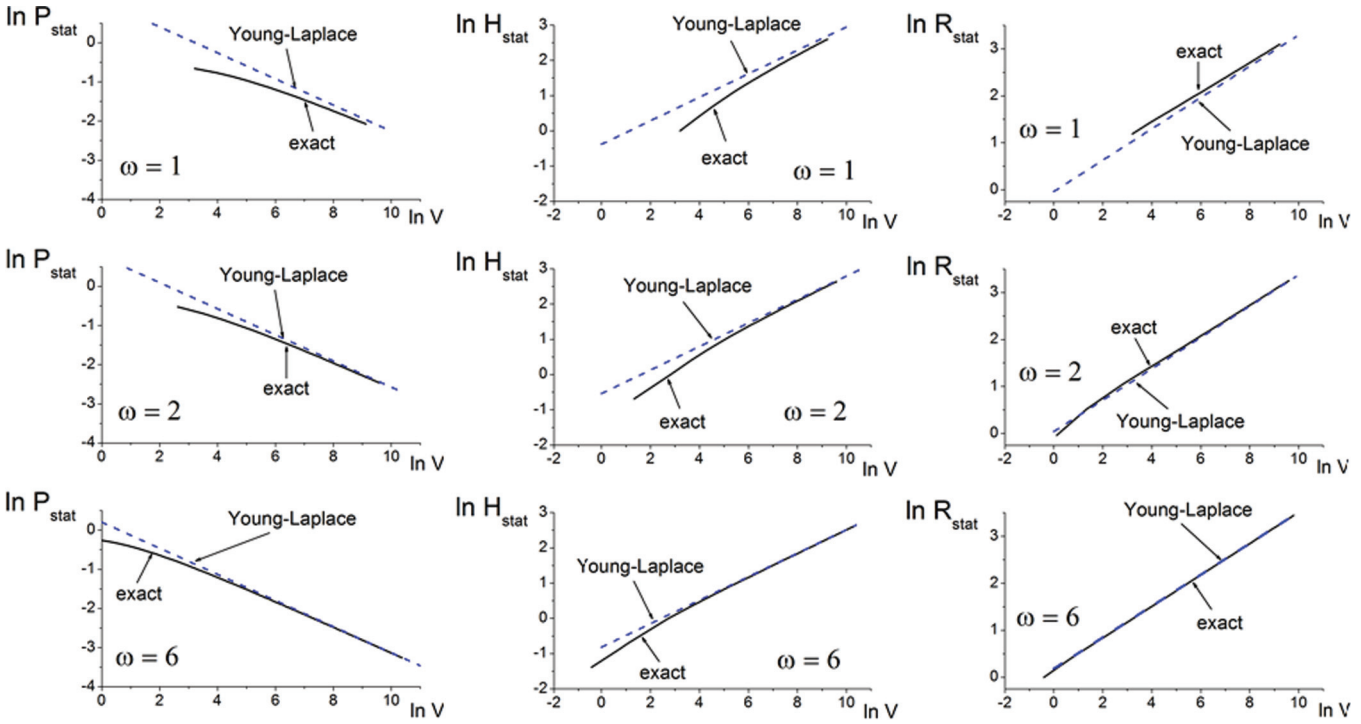

FIG. 10. (Color online) Our numerical results for the functions $P_{\rm stat}(V)$, $H_{\rm stat}(V)$, and $R_{\rm stat}(V)$ for the rescaled model with $\omega = 1$,2, and 6. The dashed line is the corresponding result in the Young-Laplace model; see Eqs. (2.57)–(2.59).

of the same height H [given by Eq. (2.39)]. Finally we display, in Fig. 11(d), the quantity

$$\frac{V_{\rm stat}^{\rm Young}(H)}{V_{\rm stat}(H)}, \tag{4.12}$$

being the ratio between the Young-Laplace model volume of the cluster with the height H and the true volume of the cluster with the same height H. The ratios in Eqs. (4.10)–(4.12) all approach 1 in the limit of infinite cluster height H. However, for a finite H, these ratios are all smaller than 1, and this effect is especially prominent for dewetting potentials with smaller values of ω such as $\omega = 1$ and $\omega = 2$. On the other side, for a large $\omega = 6$ (essentially, a short dewetting range potential), *all* these ratios in Eqs. (4.10)–(4.12) quickly approach 1, i.e., the Young-Laplace limit.

The results in Fig. 11 are in accord with the Sec. III simulation results, indicating that the deviations from the Young-Laplace model are larger for smaller values of ω, i.e., for longer ranged dewetting interactions. Thus, for example, Fig. 8 of Sec. III shows that, in contrast to Eq. (4.1) but in accord with Fig. 11(b), the ratio $2H/R$ is, at early times, significantly smaller than the Young angle slope, especially for smaller values of ω, i.e., for longer range dewetting interactions. As documented in Fig. 8 of Sec. III, this effect is correlated with the magnitude of the departures of the coarsening exponents from their asymptotic values, which are larger for smaller values of ω, i.e., for the longer range interactions. This dynamical effect will be discussed in the next section (Sec. V), in which the results of the present section are used as inputs to a cluster coarsening dynamics theory capable of analytically explaining the results of Sec. III simulations as well as the related results from the experiments such as those of Ref. [13].

B. Representation of cluster size-dependent properties

By the procedure discussed in Sec. IV A, the functions $P_{\rm stat}(V), H_{\rm stat}(V)$, and $R_{\rm stat}(V)$, displayed in Fig. 10, are numerically obtained for a discrete set of V values. However, for the purposes of Sec. V, we need these functions as functions of a continuous V, for each of the studied long range dewetting potentials. For this purpose, we fitted our numerical results for $P_{\rm stat}(V), H_{\rm stat}(V)$, and $R_{\rm stat}(V)$ with suitably chosen continuous functions. Rather than using P, H, and R as functions of V, in the mathematical framework of Sec. V it is more natural to employ a change of variables and express

$$\bar{P} = \ln(P), \quad \bar{H} = \ln(H), \quad \bar{R} = \ln(R), \tag{4.13}$$

as functions of

$$\bar{V} = \ln(V). \tag{4.14}$$

We fitted our numerical results from Sec. IV A using the four-parameter fits of the form

$$\begin{aligned} \bar{P} &= A_P^{(0)} + A_P^{(1)}\bar{V} + \left(B_P^{(0)} + B_P^{(1)}\bar{V}\right)\exp(-\bar{V}/3), \\ \bar{H} &= A_H^{(0)} + A_H^{(1)}\bar{V} + \left(B_H^{(0)} + B_H^{(1)}\bar{V}\right)\exp(-\bar{V}/3), \\ \bar{R} &= A_R^{(0)} + A_R^{(1)}\bar{V} + \left(B_R^{(0)} + B_R^{(1)}\bar{V}\right)\exp(-\bar{V}/3). \end{aligned} \tag{4.15}$$

In Eq. (4.15), the terms with the A constants are motivated by the Young-Laplace large-V limit; see Eqs. (2.57) through (2.59). In this limit, the terms in (4.15) with the B constants would represent the asymptotic corrections to the leading order

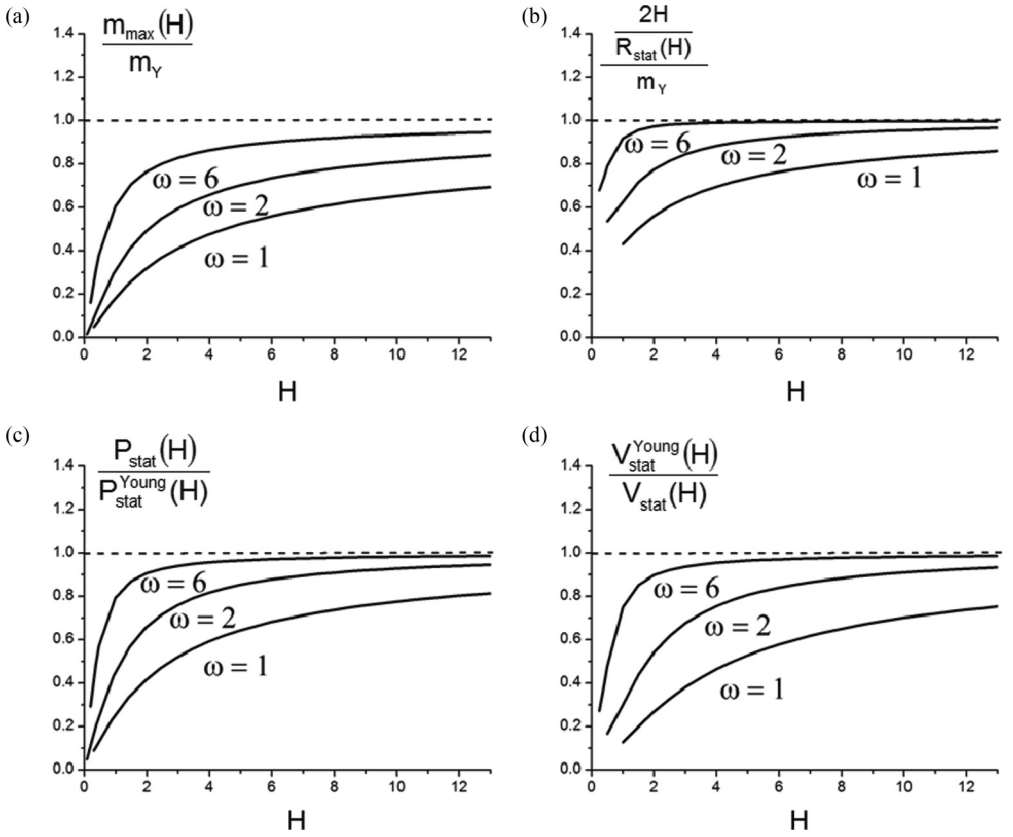

FIG. 11. The panels document the way how the four cluster properties in Eqs. (4.9) through (4.12) approach the Young-Laplace limit (the dashed line in the above figures) with increasing cluster height H, for the rescaled model with $\omega = 1,2$, and 6.

terms, while, by Eqs. (2.57)–(2.59), the A constants in the leading order terms in (4.15) would have to be fixed to

$$A_P^{(1)} = -\tfrac{1}{3}, \quad A_H^{(1)} = \tfrac{1}{3}, \quad A_R^{(1)} = \tfrac{1}{3},$$
$$A_P^{(0)} = \ln(C_P), \quad A_H^{(0)} = \ln(C_H), \quad A_R^{(0)} = \ln(C_R). \tag{4.16}$$

Thus, in the large-V limit, the A constants are fixed and Eqs. (4.15) reduce to two-parameter fits, for the B constants only. On the other hand, in our Sec. V analytic calculations, we are interested to compare analytic results with the results obtained from the simulations of Sec. III. In these simulations, the cluster volumes are below the large-V range in which Eq. (4.16) applies. For this reason, Eqs. (4.15) are considered as true four-parameter fits that are done in the actual finite V range encountered in the simulations. Using this procedure we have obtained excellent fits to the analytic results displayed in Fig. 10. These fits are used in the Sec. V calculations.

V. ANALYTIC THEORY OF THE CLUSTER COARSENING GROWTH

A. Cluster dynamics and statistics

In this section, we use the results of the Sec. IV analysis to develop a powerful cluster dynamics theory capable of analytically explaining the findings of our simulations. Main result of this section is that the *effective cluster growth coarsening exponents can be expressed as functions of the cluster size*. We calculate these exponents by our analytic approach and compare them with the results obtained from our numerical simulations of Sec. III. We find a very good agreement between our analytic results and the corresponding results for the effective exponents obtained from our simulations. This agreement is the final proof of our assertion that the long range dewetting interactions are responsible for the significant early time departures from the asymptotic predictions based on the classical Young-Laplace model.

We begin our discussion by considering in more detail the dynamics of clusters. A simple model for this dynamics was introduced already in Sec. II E. By Eqs. (2.40) and (2.44′), we have (for $D = 2$) the following result for the dynamics of cluster volume V,

$$\frac{dV}{dt} = -2\pi\Gamma\Omega\frac{P(r=R) - P(r=\xi)}{\ln(\xi/R)}, \tag{5.1}$$

with $\Gamma = \Gamma(h_{\min}) \approx \mu_{\rm sub} h_{\min} = \mu_{\rm sub}\Omega n_{\min} = D_{\rm sub}\Omega n_{\min}/k_BT$ [see the discussion above Eq. (2.43)]. By the discussions of Sec. II E, the $P(r = R)$ in Eq. (5.1) can be identified with the quasistatic cluster pressure, expressible (by the results of Sec. IV; see Fig. 10 therein) as a function of the cluster volume, $P_{\rm stat}(V)$. In addition, by the Sec. IV discussions (see Fig. 10), the cluster radius entering Eq. (5.1) is also expressible as a function of cluster volume, $R_{\rm stat}(V)$. We handle Eq. (5.1) in the spirit of the statistical mean-field Lifshits-Slyozov theory [8,16,17], so Eq. (5.1) will be replaced by the

equation

$$\frac{dV}{dt} = F(V) = -2\pi\Gamma\Omega\frac{P_{\rm stat}(V) - P^*}{\ln[\xi/R_{\rm stat}(V)]}. \tag{5.2}$$

In Eqs. (5.1) and (5.2), the length scale ξ is a "screening length" proportional to the average intercluster separation λ; see Sec. II E and Ref. [35]. The P^* in Eq. (5.2) is discussed in the following. The volume conservation law implied by Eq. (2.1) ensures that the average cluster volume is equal to the film volume initially (at $t = 0$) covering the area $= \pi(\lambda/2)^2$. Thus, we have

$$\langle V\rangle = \pi\left(\frac{\lambda}{2}\right)^2\tilde{h}_0, \tag{5.3}$$

where $\tilde{h}_0$ labels the initial film thickness measured above the dry level $h_{\rm min}$ (see Secs. III A and IV A). By Eq. (5.3), we can write

$$\xi = C\lambda = C\sqrt{\frac{4\langle V\rangle}{\pi\tilde{h}_0}}, \tag{5.4}$$

where C is a numerical proportionality constant discussed in the following (see Sec. V F).

Within the Lifshits-Slyozov statistical approach, the ensemble of clusters is described by their volumes distribution function $\rho(V,t)$ such that $\rho(V,t)dV = dN =$ the number of clusters within the volume interval $(V,V+dV)$. Thus, the total number of clusters is

$$N = \int dN = \int dV\rho(V,t). \tag{5.5}$$

The total film volume $V_{\rm film}$ is essentially all within the clusters. Thus,

$$V_{\rm film} = \int dNV = \int dV\rho(V,t)V. \tag{5.6}$$

The average cluster volume is then given by

$$\langle V\rangle = \frac{V_{\rm film}}{N} = \int dV\pi(V,t)V. \tag{5.7}$$

Here,

$$\pi(V,t) = \frac{\rho(V,t)}{N} \tag{5.8}$$

is the cluster volume probability density function. The time evolution of the cluster distribution function $\rho(V,t)$ is, in general, governed by the continuity equation,

$$\frac{\partial}{\partial t}\rho(V,t) = -\frac{\partial}{\partial V}[F(V)\rho(V,t)]. \tag{5.9}$$

Here, in our case, the function $F(V)$ is given by Eq. (5.2). The conservation of the total film volume Eq. (5.6), implies a restriction on the possible form of $F(V)$ that can be used to fix the value of the parameter P^* introduced in Eq. (5.2). Indeed, by using Eqs. (5.6) and (5.9), it is easy to show that the condition $dV_{\rm film}/dt = 0$ implies the condition

$$0 = \langle F(V)\rangle = \int dV\pi(V,t)F(V). \tag{5.10}$$

In combination with the form of $F(V)$ in Eq. (5.2), Eq. (5.10) can be easily used to obtain the value of the parameter P^*.

B. Cluster distribution cutoff

A special feature of the here interesting cluster distributions is that they exhibit a sharp cutoff $V_{\rm max}(t)$ (the maximum cluster size) such that

$$\rho(V,t) = 0, \quad \text{for} \quad V > V_{\rm max}(t). \tag{5.11}$$

The cutoff $V_{\rm max}(t)$ will play an essential role in the following discussions. Within the present kinetic theory Eq. (5.9), the presence of the sharp distribution cutoff imposes a special requirement, namely the consistency condition noted for the first time by Lifshits and Slyozov [8,9] for the system they considered. This condition, generalized to an $F(V)$ of a general form (see Appendix B), requires that

$$\left(F(V) - V\frac{\partial F(V)}{\partial V}\right)_{V=V_{\rm max}(t)} = 0, \tag{5.12}$$

which is easily seen to be equivalent to

$$\left.\frac{\partial\ln[F(V)]}{\partial\ln(V)}\right|_{V=V_{\rm max}} = 1. \tag{5.12$'$}$$

A consequence of the condition Eq. (5.12) is that the cutoff size dynamics equation,

$$\frac{dV_{\rm max}}{dt} = F(V_{\rm max}), \tag{5.13}$$

can also be written as

$$\frac{dV_{\rm max}}{dt} = \left(V\frac{\partial F(V)}{\partial V}\right)_{V=V_{\rm max}}. \tag{5.14}$$

To proceed with discussing the dynamics of $V_{\rm max}(t)$, we simplify our kinetic theory by using the approximation (valid for $V \sim V_{\rm max}$),

$$\begin{aligned} F(V) &= -2\pi\Gamma\Omega\frac{P_{\rm stat}(V) - P^*}{\ln[\xi/R_{\rm stat}(V)]} \\ &\approx -2\pi\Gamma\Omega\frac{P_{\rm stat}(V) - P^*}{\ln[\xi/R_{\rm stat}(V_{\rm max})]}, \end{aligned} \tag{5.15}$$

within which Eq. (5.10) yields the result

$$P^* = \langle P_{\rm stat}(V)\rangle, \tag{5.16}$$

while Eq. (5.12) reduces to

$$P^* = P_{\rm stat}(V_{\rm max}) - V_{\rm max}\frac{dP_{\rm stat}(V_{\rm max})}{dV_{\rm max}}. \tag{5.17}$$

By Eqs. (5.15) and (5.14), we obtain an equation giving the dynamics of $V_{\rm max}(t)$, of the form

$$\frac{dV_{\rm max}}{dt} = \frac{V_{\rm max}}{\tau(V_{\rm max})}, \tag{5.18}$$

with a conveniently defined $V_{\rm max}$-dependent time scale,

$$\frac{1}{\tau(V_{\rm max})} = 2\pi\Gamma\Omega\frac{-\left(\frac{dP_{\rm stat}(V)}{dV}\right)_{V=V_{\rm max}}}{\ln\left(\frac{\xi}{R_{\rm stat}(V_{\rm max})}\right)}. \tag{5.19}$$

We recall that, by Eq. (5.4), the length scale ξ in the above equation is given by

$$\xi = C\lambda = C\sqrt{\frac{4\langle V\rangle}{\pi\tilde{h}_0}}. \tag{5.20}$$

Equations (5.18) through (5.20) will form a closed description of the dynamics of $V_{\max}$ provided we manage to express the $\langle V\rangle$ [entering Eq. (5.20)] as a function of $V_{\max}$. If this closing is achievable, then the right hand side of the first order differential equation (5.18) would become a function of $V_{\max}$ only. Such an equation can be then directly integrated. The result would give the time evolution of the cutoff $V_{\max}$.

C. Closing the cutoff dynamics equation

Fortunately, the above anticipated closing of the cutoff dynamics equation (5.18) is indeed possible. We base it on the approximate relation

$$\langle P_{\rm stat}(V)\rangle \approx P_{\rm stat}(\langle V\rangle). \tag{5.21}$$

For our system, the relation in Eq. (5.21) is indeed satisfied to a very good approximation. We document this in Fig. 12 from our simulations, which plots the obtained average cluster pressure $\langle P\rangle$ versus the average cluster volume $\langle V\rangle$, obtained at various times. In the same figure, we give also the function $P_{\rm stat}(V)$ as obtained in our analytic calculations discussed in Sec. IV (see Fig. 10 therein). From Fig. 12 one can see that Eq. (5.21) holds for essentially all times during the interface evolution stage characterized by the presence of growing clusters depicted in Fig. 4(b).

By Eq. (5.21) in combination with Eqs. (5.16) and (5.17), we obtain the relation

$$P^* = P_{\rm stat}(\langle V\rangle) = P_{\rm stat}(V_{\max}) - V_{\max}\frac{dP_{\rm stat}(V_{\max})}{dV_{\max}}; \tag{5.22}$$

i.e.,

$$P^* = P_{\rm stat}(\langle V\rangle) = P_{\rm stat}(V_{\max})\cdot\left[1 - \frac{d\ln[P_{\rm stat}(V_{\max})]}{d\ln(V_{\max})}\right]. \tag{5.22$'$}$$

By Eq. (5.22),

$$\langle V\rangle = P_{\rm stat}^{-1}\left[P_{\rm stat}(V_{\max}) - V_{\max}\frac{dP_{\rm stat}(V_{\max})}{dV_{\max}}\right]. \tag{5.23}$$

Here, the $P_{\rm stat}^{-1}$ signifies the *inverse* function of the function $P_{\rm stat}(V)$. Note that by Eq. (5.23), we managed to express the average cluster volume $\langle V\rangle$ [entering Eq. (5.20)] as a function $V_{\max}$.

In combination with Eq. (5.23), Eqs. (5.18) through (5.20) form a closed description for the dynamics of $V_{\max}$. The right hand side of the first order differential equation (5.18) thus becomes a function of $V_{\max}$ only and can be thus integrated. The result of this integration gives the time evolution of $V_{\max}$ through the integral,

$$t = \int^{V_{\max}}\frac{dV}{V}\tau(V) = \int^{V_{\max}} d\ln(V)\tau(V), \tag{5.24}$$

Here, by Eqs. (5.19), (5.20), and (5.23),

$$\tau(V) = \left[2\pi\Gamma\Omega\frac{-\frac{dP_{\rm stat}(V)}{dV}}{\ln\left(\frac{\xi(V)}{R_{\rm stat}(V)}\right)}\right]^{-1}, \tag{5.25}$$

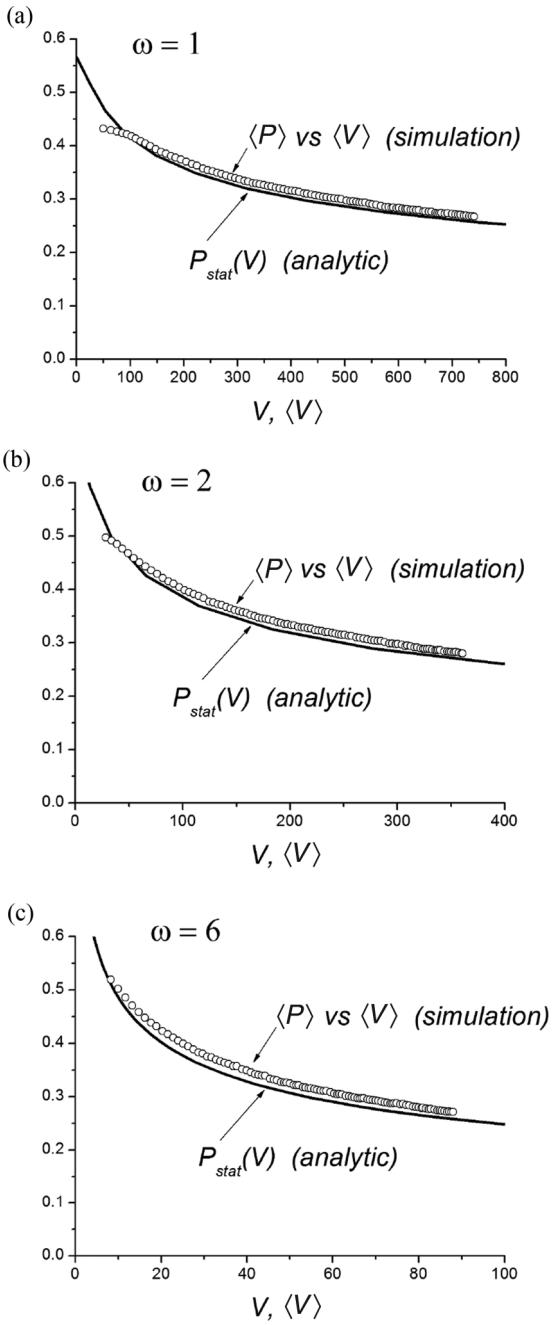

FIG. 12. (a) The figure contains two plots. One of them is obtained from our simulations of the model with $\omega = 1$, in $D = 2$. It plots the obtained average cluster pressure $\langle P\rangle$ versus the average cluster volume $\langle V\rangle$, obtained at various times. In the same figure, we give also the plot displaying the function $P_{\rm stat}(V)$ as obtained in our analytic calculations in Sec. IV, for $\omega = 1$, in $D = 2$ (see Fig. 10 in Sec. IV). From the displays of the two plots, one can see that Eq. (5.21) holds for essentially all times (except for very early times, when the clusters are small and not quasistatic). Panel (b) is the same as the panel (a) but for the model with $\omega = 2$, in $D = 2$. Panel (c) is the same as the panel (a) but for the model with $\omega = 6$, in $D = 2$.

with

$$\xi(V) = C\sqrt{\frac{4P_{\rm stat}^{-1}\left[P_{\rm stat}(V) - V\frac{dP_{\rm stat}(V)}{dV}\right]}{\pi\tilde{h}_0}}. \tag{5.26}$$

Equation (5.24) gives the system evolution time t as a function of $V_{\max}$. Inverting this function thus gives the $V_{\max}$ as function of the time t. Thus, Eq. (5.24), in combination with Eqs. (5.25) and (5.26), provide the desired solution $V_{\max}(t)$ for the evolution of the cluster distribution cutoff, i.e., of the maximum cluster size.

D. Calculating the effective coarsening exponents

A neat feature of Eq. (5.24) is that it can be used to obtain the effective exponents of the cluster coarsening growth. Interestingly, as discussed in the following, these effective coarsening exponents can be expressed as functions of cluster size, e.g., as functions of cluster average volume $\langle V\rangle$ at any time t. This is one of the major results of this study.

To derive this significant result, we first discuss the effective coarsening exponent for the growth of the cutoff, i.e., the maximum cluster size $V_{\max}(t)$,

$$\beta_{V_{\max}} = \frac{d\ln(V_{\max})}{d\ln(t)}. \tag{5.27}$$

By Eq. (5.27),

$$\beta_{V_{\max}} = \frac{1}{\frac{d\ln(t)}{d\ln(V_{\max})}} = \frac{t}{\frac{dt}{d\ln(V_{\max})}}. \tag{5.27$'$}$$

Using here Eq. (5.24), we obtain

$$\beta_{V_{\max}} = \frac{\int^{V_{\max}} d\ln(V)\tau(V)}{\tau(V_{\max})}. \tag{5.28}$$

By Eq. (5.28), it is easy to see that

$$\frac{d}{d\ln(V_{\max})}[\tau(V_{\max})\beta_{V_{\max}}] = \tau(V_{\max}). \tag{5.29}$$

After a little algebra, Eq. (5.29) can be transformed into the differential equation,

$$\frac{d\beta_{V_{\max}}}{d\ln(V_{\max})} + \frac{1}{\beta^{(0)}_{V_{\max}}}\beta_{V_{\max}} = 1, \tag{5.30}$$

with

$$\frac{1}{\beta^{(0)}_{V_{\max}}} = \frac{d\ln[\tau(V_{\max})]}{d\ln(V_{\max})}. \tag{5.31}$$

Note that solving the differential equation (5.30) effectively gives the desired effective coarsening $\beta_{V_{\max}}$ expressed as function of $V_{\max}$. It is convenient to re-express Eq. (5.30) as

$$\beta_{V_{\max}} = \beta^{(0)}_{V_{\max}}(V_{\max})\cdot\left[1 - \frac{d\beta_{V_{\max}}}{d\ln(V_{\max})}\right]. \tag{5.32}$$

The $\beta_{V_{\max}}$ and other effective coarsening exponents are slowly changing functions of $V_{\max}$ (as documented in the following sections), so Eq. (5.32) can be solved iteratively by writing

$$\beta^{(n)}_{V_{\max}}(V_{\max}) = \beta^{(0)}_{V_{\max}}(V_{\max})\cdot\left[1 - \frac{d\beta^{(n-1)}_{V_{\max}}(V_{\max})}{d\ln(V_{\max})}\right],$$
$$n = 1,2,3,\ldots, \tag{5.33}$$

with $\beta^{(0)}_{V_{\max}}$ in Eq. (5.31) being the zeroth order approximation. From the concrete calculations discussed in Sec. V F, we find that Eq. (5.33) is a rapidly converging iteration. The effective coarsening exponent,

$$\beta_{V_{\max}}(V_{\max}) = \lim_{n\to\infty}\beta^{(n)}_{V_{\max}}(V_{\max}), \tag{5.34}$$

is well approximated already by $\beta^{(n=3)}_{V_{\max}}(V_{\max})$. Importantly, by the above discussions, thus obtained effective coarsening exponent $\beta_{V_{\max}}$ is expressed as a function of $V_{\max}$. This exponent can be expressed also as a function of the average cluster volume $\langle V\rangle$. This can be accomplished by using Eq. (5.23) relating the $\langle V\rangle$ to $V_{\max}$. In practice, this can be done by making the parametric plot of $\beta_{V_{\max}}$ versus $\langle V\rangle$, with both of these variables expressed as functions of $V_{\max}$.

Once the $\beta_{V_{\max}}$ is calculated, other coarsening exponents can be also calculated in a straightforward fashion. Thus, the exponent for the growth of the average cluster volume,

$$\beta_{\langle V\rangle} = \frac{d\ln(\langle V\rangle)}{d\ln(t)}, \tag{5.35}$$

can be expressed as

$$\beta_{\langle V\rangle} = \frac{d\ln(\langle V\rangle)}{d\ln(V_{\max})}\cdot\frac{d\ln(V_{\max})}{d\ln(t)}; \tag{5.36}$$

i.e.,

$$\beta_{\langle V\rangle} = \frac{d\ln(\langle V\rangle)}{d\ln(V_{\max})}\cdot\beta_{V_{\max}}(V_{\max}). \tag{5.37}$$

Here, the first term is a function of $V_{\max}$ that can be calculated using Eq. (5.23) expressing $\langle V\rangle$ as function of $V_{\max}$. Thus, Eq. (5.37) gives the exponent $\beta_{\langle V\rangle}$ as function of $V_{\max}$.

It is, however, more natural to express this exponent as a function of the average cluster volume $\langle V\rangle$. This can be accomplished by using Eq. (5.23) relating the $\langle V\rangle$ to $V_{\max}$. In practice, this can be done by making the parametric plot of $\beta_{\langle V\rangle}$ versus $\langle V\rangle$, with both variables expressed as functions of $V_{\max}$.

Within our theory, it is also possible to calculate the exponents associated with the coarsening dynamics of other quantities characterizing the ensemble of clusters, such as average cluster pressure, cluster height, and cluster base radius. Thus, for the average cluster pressure we have, by Eq. (5.21),

$$\langle P\rangle = \langle P_{\text{stat}}(V)\rangle \approx P_{\text{stat}}(\langle V\rangle), \tag{5.38}$$

So, the pressure exponent,

$$\beta_{\langle P\rangle} = \frac{d\ln(\langle P\rangle)}{d\ln(t)} \approx \frac{d\ln[P_{\text{stat}}(\langle V\rangle)]}{d\ln(t)}, \tag{5.39}$$

can be calculated as

$$\beta_{\langle P\rangle} = \frac{d\ln[P_{\text{stat}}(\langle V\rangle)]}{d\ln(\langle V\rangle)}\cdot\frac{d\ln\langle V\rangle}{d\ln(t)},$$

i.e.,

$$\beta_{\langle P\rangle} = \frac{d\ln[P_{\text{stat}}(\langle V\rangle)]}{d\ln(\langle V\rangle)}\cdot\beta_{\langle V\rangle}. \tag{5.40}$$

In Eq. (5.40), the $\beta_{\langle V\rangle}$ is calculated as described before, while the first term can be calculated by using the results of Sec. IV for the pressure $P_{\text{stat}}(V)$ of the quasistatic clusters (see Fig. 10

and Sec. IV B). In effect, Eq. (5.40) thus gives the exponent $\beta_{\langle P\rangle}$ expressed as a function of the cluster average volume $\langle V\rangle$.

The coarsening exponents for growth of average cluster height and base radius are obtained using the relations

$$\langle H\rangle \approx H_{\rm stat}(\langle V\rangle), \quad \langle R\rangle \approx R_{\rm stat}(\langle V\rangle), \tag{5.41}$$

with the functions $H_{\rm stat}$ and $R_{\rm stat}$ calculated in Sec. IV (see Fig. 10 and Sec. IV B). By Eq. (5.41),

$$\begin{aligned}\beta_{\langle H\rangle} &= \frac{d\ln(\langle H\rangle)}{d\ln(t)} \approx \frac{d\ln[H_{\rm stat}(\langle V\rangle)]}{d\ln(\langle V\rangle)}\cdot\frac{d\ln\langle V\rangle}{d\ln(t)}\\ &= \frac{d\ln[H_{\rm stat}(\langle V\rangle)]}{d\ln(\langle V\rangle)}\cdot\beta_{\langle V\rangle}\end{aligned} \tag{5.42}$$

and

$$\begin{aligned}\beta_{\langle R\rangle} &= \frac{d\ln(\langle R\rangle)}{d\ln(t)} \approx \frac{d\ln[R_{\rm stat}(\langle V\rangle)]}{d\ln(\langle V\rangle)}\cdot\frac{d\ln\langle V\rangle}{d\ln(t)}\\ &= \frac{d\ln[R_{\rm stat}(\langle V\rangle)]}{d\ln(\langle V\rangle)}\cdot\beta_{\langle V\rangle}.\end{aligned} \tag{5.43}$$

Thus, once the exponent $\beta_{\langle V\rangle}$ is calculated (as described before), Eqs. (5.42) and (5.43) can be then used to calculate the exponents for the growth of the cluster average height and base radius. In Sec. V F, we employ the theory we developed in this and previous sections to derive various coarsening exponents for the clusters emerging in our interface dynamics model of Sec. II, with the functions $P_{\rm stat}(V), H_{\rm stat}(V)$, and $R_{\rm stat}(V)$ calculated in Sec. IV (see Fig. 10 and Sec. IV B). Prior to this, in the next section, we first revisit the Young-Laplace model, Sec. II E.

Finally, it should be stressed that, within the present theory, the size-dependent coarsening exponents do not depend on the value of the transport coefficient Γ entering the cluster volume dynamics Eqs. (5.18) and (5.19). From these equations and Eq. (5.28), one can easily see that Γ cancels out in the final expression for the size-dependent coarsening exponent.

E. Young-Laplace model revisited

As an important illustration for the theoretical program developed in the previous section, we first apply it to Young-Laplace model discussed in Sec. II E. This model is interesting in its own right since it gives asymptotic behavior of the coarsening process at the longest time scales. In the Young-Laplace limit, we have (for $D = 2$)

$$\begin{aligned}&H_{\rm stat}^{\rm Young}(V) = C_H V^{1/3}, \quad R_{\rm stat}^{\rm Young}(V) = C_R V^{1/3},\\ &P_{\rm stat}^{\rm Young}(V) = C_P V^{-1/3},\end{aligned} \tag{5.44}$$

with C_H, C_R, and C_P being numerical constants expressible in terms of the Young angle slope; see Eqs. (2.57)–(2.59) of Sec. II. By Eq. (5.44), in combination with Eq. (5.22′) we have

$$\langle V\rangle^{-1/3} = V_{\rm max}^{-1/3}\cdot[1-(-1/3)];$$

i.e.,

$$\langle V\rangle = \left(\frac{3}{4}\right)^3 V_{\rm max}. \tag{5.45}$$

Next, using Eq. (5.44) in combination with Eqs. (5.25) and (5.26), we have

$$\tau(V) = AV^{4/3}\ln\left(K\frac{V^{1/3}}{\tilde{h}_0}\right), \tag{5.46}$$

with the numerical constants

$$K = \frac{4}{\pi}\left(\frac{3}{4}\right)^3\frac{C^2}{C_R^2}, \quad A = \frac{3}{2C_P}\cdot\frac{1}{2\pi\Gamma\Omega}. \tag{5.47}$$

By Eqs. (5.46) and (5.28), after an elementary integration, we find

$$\beta_{V_{\rm max}} = \frac{3}{4}\cdot\left(1-\frac{1}{4\cdot\ln\left[KV_{\rm max}^{1/3}/\tilde{h}_0\right]}\right) \tag{5.48}$$

or, by Eq. (5.45),

$$\beta_{V_{\rm max}} = \frac{3}{4}\cdot\left(1-\frac{1}{4\cdot\ln[(4K/3)\langle V\rangle^{1/3}/\tilde{h}_0]}\right). \tag{5.49}$$

By Eq. (5.45) we have,

$$\beta_{\langle V\rangle} = \beta_{V_{\rm max}}. \tag{5.50}$$

Thus, by Eq. (5.49),

$$\beta_{\langle V\rangle} = \frac{3}{4}\cdot\left(1-\frac{1}{4\cdot\ln[(4K/3)\langle V\rangle^{1/3}/\tilde{h}_0]}\right). \tag{5.51}$$

Next, by Eqs. (5.40), (5.42), and (5.43), in combination with Eq. (5.44), we have

$$\beta_{\langle P\rangle} = -\tfrac{1}{3}\beta_{\langle V\rangle}, \quad \beta_{\langle H\rangle} = \beta_{\langle R\rangle} = \tfrac{1}{3}\beta_{\langle V\rangle}. \tag{5.52}$$

Thus, by Eqs. (5.51) and (5.52), we find

$$\beta_{\langle P\rangle} = -\frac{1}{4}\cdot\left(1-\frac{1}{4\cdot\ln[(4K/3)\langle V\rangle^{1/3}/\tilde{h}_0]}\right), \tag{5.53}$$

and

$$\beta_{\langle H\rangle} = \beta_{\langle R\rangle} = \frac{1}{4}\cdot\left(1-\frac{1}{4\cdot\ln[(4K/3)\langle V\rangle^{1/3}/\tilde{h}_0]}\right). \tag{5.54}$$

By the above results,

$$\lim_{\langle V\rangle\to\infty}\beta_{\langle H\rangle} = \lim_{\langle V\rangle\to\infty}\beta_{\langle R\rangle} = \frac{1}{4}, \tag{5.55}$$

whereas

$$\lim_{\langle V\rangle\to\infty}\beta_{\langle V\rangle} = \frac{3}{4}, \tag{5.56}$$

and

$$\lim_{\langle V\rangle\to\infty}\beta_{\langle P\rangle} = -\frac{1}{4}. \tag{5.57}$$

By the results in Eqs. (5.51) and (5.54), we see that the magnitudes of the effective ($\langle V\rangle$−dependent) coarsening exponents $\beta_{\langle V\rangle}$ $\beta_{\langle H\rangle}$ and $\beta_{\langle R\rangle}$ are depressed below their asymptotic values, by a slowly changing logarithmic correction. The correction originates from the log in the denominator of the cluster dynamics equation (5.15), containing the "screening length" ξ. This depression of the exponents *below* their asymptotic values is the dominant correction to scaling at *long* times, i.e., in the large $\langle V\rangle$ limit. On the other hand, as we

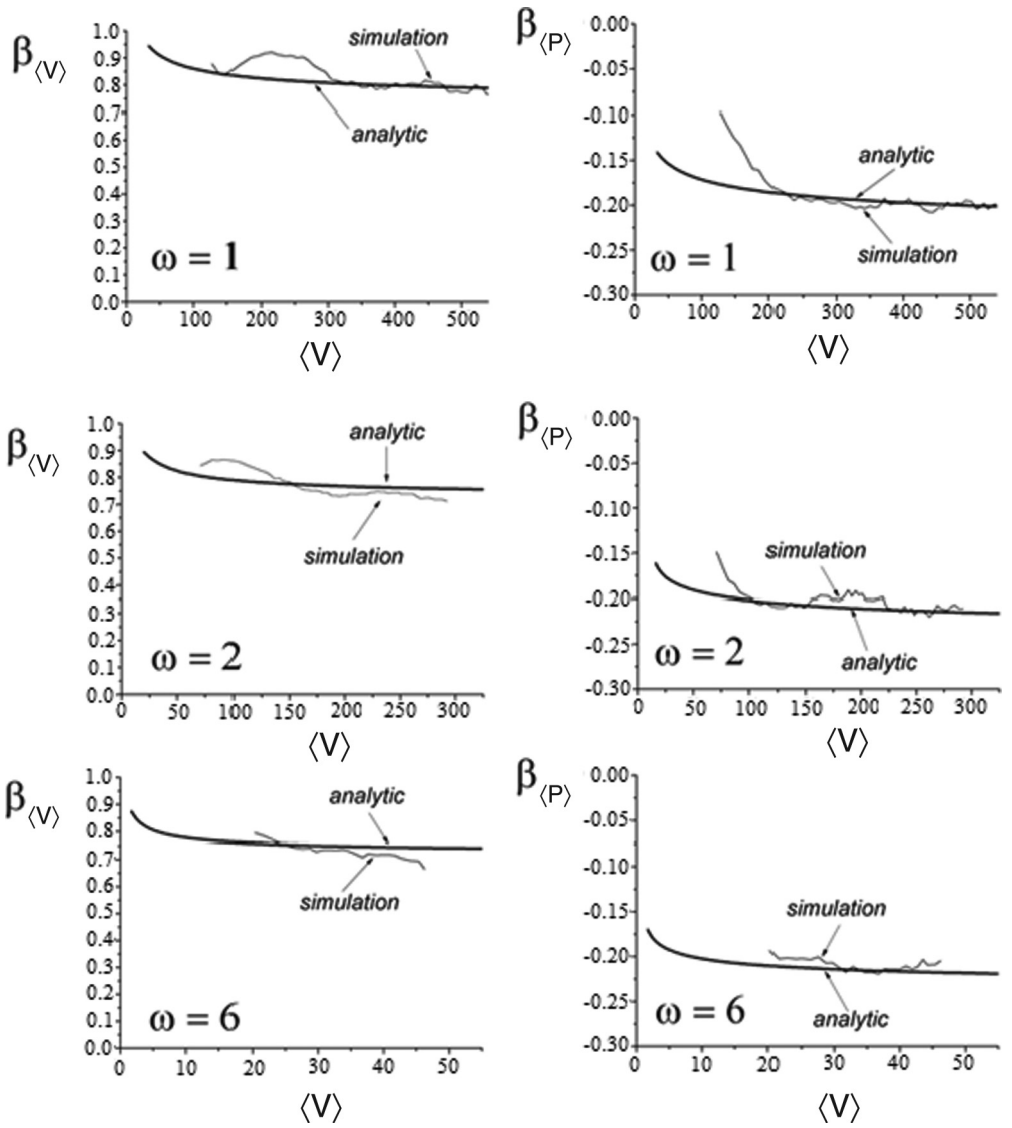

FIG. 13. Analytic results versus the corresponding simulation results for the effective coarsening exponents for the growth of cluster volume, $\beta_{\langle V\rangle}$, and for the cluster pressure, $\beta_{\langle P\rangle}$, as functions of the average cluster volume $\langle V\rangle$. We recall that the asymptotic value of $\beta_{\langle V\rangle}$ is 0.75, whereas the asymptotic value of $\beta_{\langle P\rangle}$ is -0.25, for infinite $\langle V\rangle$.

reveal in the following section (Sec. V F), at *early* times, the dominant correction to scaling comes from the breakdown of Eq. (5.44), i.e., of the classical Young-Laplace model. In this early time regime Eq. (5.44) needs to be replaced by the exact forms of $P_{\rm stat}(V), H_{\rm stat}(V)$, and $R_{\rm stat}(V)$ obtained in Sec. IV. The resulting coarsening exponents are discussed in the next section (Sec. V F). Here we note that the breakdown of the Young-Laplace model at early times yields the coarsening exponents that are actually *above* their asymptotic values, in contrast to the effect of the above discussed logarithmic correction (due to the screening length ξ) which [by Eqs. (5.51) and (5.54)] tends to depress the coarsening exponents $\beta_{\langle V\rangle}$ $\beta_{\langle H\rangle}$ and $\beta_{\langle R\rangle}$ below their asymptotic values. Thus, these exponents eventually approach their asymptotic values *from below*. In contrast to this, by Eq. (5.53), the pressure exponent $\beta_{\langle P\rangle}$ approaches *from above* its asymptotic value of $-1/4$. See also the discussion at the end of Sec. V F and Fig. 15 therein.

F. Effective exponents beyond the Young-Laplace model

In this section, we use the results of the previous sections to analytically explain the findings of our simulations in Sec. III. The main theoretical results will be the *effective cluster growth coarsening exponents calculated as functions of the cluster average volume* $\langle V\rangle$ *at time t*. Furthermore, we compare our analytic results for the cluster coarsening exponents with the corresponding results obtained from our numerical simulations of Sec. III. The comparison shows a very good agreement between our analytic results and the corresponding results for the effective exponents obtained from our simulations. This agreement constitutes the final proof of our assertion that the long range dewetting potentials are responsible for the significant early time departures from the asymptotic predictions based on the classical Young-Laplace model.

Our analytic calculation of the effective coarsening exponents employs the iterative procedure introduced in Eq. (5.33),

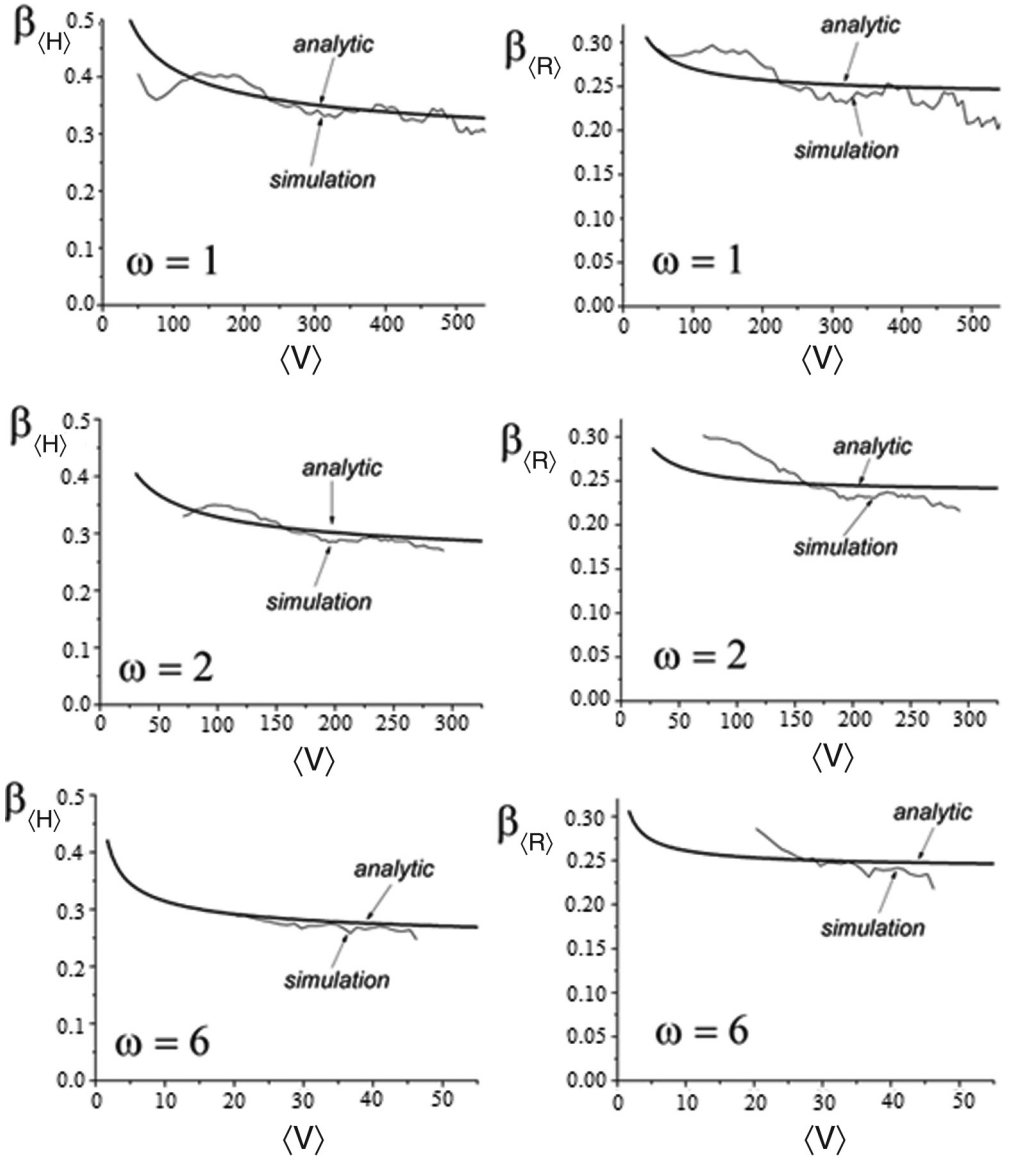

FIG. 14. Analytic results versus the corresponding simulation results for the effective coarsening exponents for the growth of cluster height, $\beta_{\langle H\rangle}$, and cluster base radius, $\beta_{\langle R\rangle}$, as functions of the average cluster volume $\langle V\rangle$. We recall that the asymptotic values of $\beta_{\langle H\rangle}$ and $\beta_{\langle R\rangle}$ are both 0.25 for infinite $\langle V\rangle$.

yielding the exponent $\beta_{V\max}$. The exponents $\beta_{\langle V\rangle}$, $\beta_{\langle P\rangle}$ $\beta_{\langle H\rangle}$, and $\beta_{\langle R\rangle}$ are then calculated using Eqs. (5.40) through (5.43) and expressed as functions of the average cluster volume $\langle V\rangle$, as detailed in Sec. V D. In these analytic calculations, the central inputs are the forms of quasistatic cluster pressure $P_{\rm stat}(V)$, cluster height $H_{\rm stat}(V)$, and cluster base radius $R_{\rm stat}(V)$, all obtained in Sec. IV for our rescaled model (Sec. II D), for the potentials with $\omega = 1$, $\omega = 2$, and $\omega = 6$; see Fig. 10 of Sec. IV and Sec. IV B. In the figures that follow, we display our analytic results for $\beta_{\langle V\rangle}$, $\beta_{\langle P\rangle}$, $\beta_{\langle H\rangle}$, and $\beta_{\langle R\rangle}$ as functions of $\langle V\rangle$, for the potentials with $\omega = 1$, $\omega = 2$, and $\omega = 6$; see Figs. 13 and 14. In these figures, for comparison, we also display the corresponding results for $\beta_{\langle V\rangle}$, $\beta_{\langle P\rangle}$ $\beta_{\langle H\rangle}$, and $\beta_{\langle R\rangle}$ as functions of $\langle V\rangle$, obtained from our simulations in Sec. III. From Figs. 13 and 14 we see that there are statistical fluctuations seen in the simulation results. Note, however, that these statistical fluctuations go *around* the corresponding analytic results for the exponents. By Figs. 13 and 14, the agreement between the analytic and the simulation results for the exponents is very good, for *all* the potentials ($\omega = 1$, $\omega = 2$, and $\omega = 6$) and for *all* the exponents $\beta_{\langle V\rangle}$, $\beta_{\langle P\rangle}$ $\beta_{\langle H\rangle}$, and $\beta_{\langle R\rangle}$.

We recall that our analytic theory contains a numerical proportionality constant C [see Eq. (5.26) or Eq. (5.20) for the screening length]. This constant relates to the intercluster transport of material over nearly dry areas where the film thickness is very small. Thus, the C should not depend much on the details of the dewetting potential such as the value of ω, which actually describes the asymptotic behavior of the potential for large film thicknesses occurring only in wet areas inside the clusters. We indeed find that Sec. III simulations of the cases $\omega = 1$, $\omega = 2$, and $\omega = 6$ can *all* be well fitted by

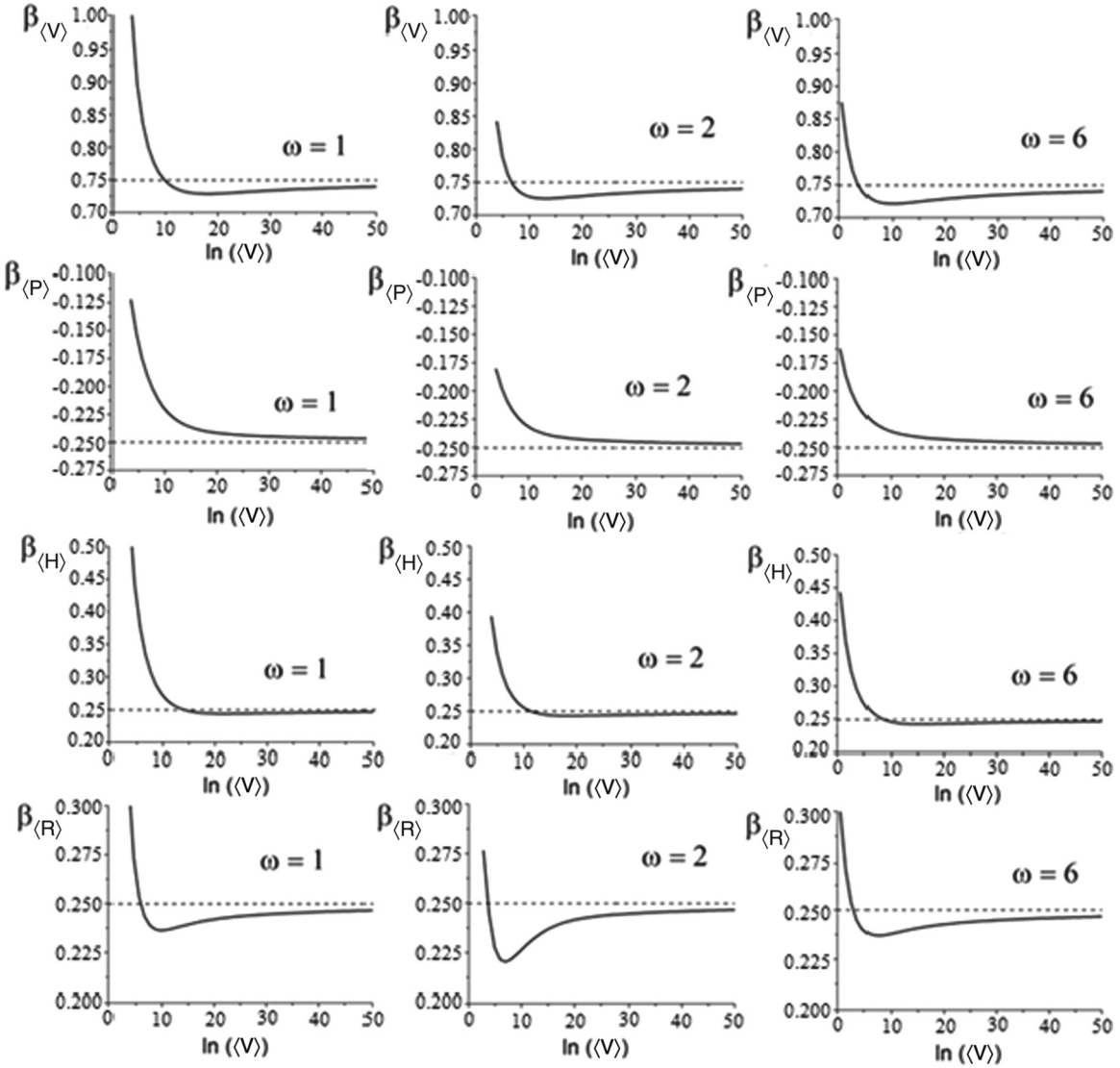

FIG. 15. Analytic results for the effective coarsening exponents $\beta_{\langle V\rangle}$, $\beta_{\langle P\rangle}$, $\beta_{\langle H\rangle}$, and $\beta_{\langle R\rangle}$ as functions of the average cluster volume $\langle V\rangle$, for the rescaled model with $\omega = 1$, 2, and 6. In this figure, we display the exponents in a volume $\langle V\rangle$ range that is much wider than in Figs. 13 and 14 so one can see clearly the approach to the asymptotic exponent values, which are 0.75 for $\beta_{\langle V\rangle}$, -0.25 for $\beta_{\langle P\rangle}$, 0.25 for $\beta_{\langle H\rangle}$, and 0.25 for $\beta_{\langle R\rangle}$.

our analytic theory using a *single* value of $C = 1.60$ that has been employed in the figures displayed in this section.

As evidenced by Figs. 13 and 14, both the analytic theory and the simulations exhibit a significant effect of the actual value of the ω on the early time behavior of the effective exponents $\beta_{\langle V\rangle}$, $\beta_{\langle P\rangle}$, $\beta_{\langle H\rangle}$, and $\beta_{\langle R\rangle}$: The larger the ω, the smaller will be the difference between effective exponents and their asymptotic values in Eqs. (5.55)–(5.57). Indeed, for a large $\omega = 6$ (essentially, a short range dewetting potential), the early time range exponent $\beta_{\langle H\rangle}$ is about 0.28, so it is close to the asymptotic $\beta_{\langle H\rangle} = 0.25$. On the other hand, for long-range potentials with for $\omega = 1$ and $\omega = 2$, the early time range exponent $\beta_{\langle H\rangle}$ is about 0.33; i.e., it deviates significantly from the asymptotic $\beta_{\langle H\rangle} = 0.25$. We recall that the cases $\omega = 1$ and $\omega = 2$ are the physically interesting cases; see Sec. I. Experimentally, as discussed in Sec. I, such an effective early time exponent, measured to be $\beta_H^{\text{eff}} \approx 0.33$, has been indeed reported in Ref. [13]. *Our analytic theory, in combination with simulations, explains these experimental findings in terms of long range dewetting potentials.*

With increasing time, i.e., cluster average volume $\langle V\rangle$, the effective coarsening exponents do approach their asymptotic values Eqs. (5.55)–(5.57) predicted by Young-Laplace model. This approach is, however, *nonmonotonous* for the exponents $\beta_{\langle V\rangle}$, $\beta_{\langle H\rangle}$, and $\beta_{\langle R\rangle}$, as can be seen in Fig. 15. In this figure, we display the analytically calculated effective exponents over a volume $\langle V\rangle$ range that is much wider than in Figs. 13 and 14, so one can see better the approach to the asymptotic values of the exponents which are 0.75 for $\beta_{\langle V\rangle}$, -0.25 for $\beta_{\langle P\rangle}$, 0.25 for $\beta_{\langle H\rangle}$, and 0.25 for $\beta_{\langle R\rangle}$. By Fig. 15, for example, the exponent $\beta_{\langle R\rangle}$ is bigger than $\frac{1}{4}$ at early times, and it crosses $\frac{1}{4}$ at a *finite* time. After this, the $\beta_{\langle R\rangle}$ becomes smaller than $\frac{1}{4}$, and it goes through a minimum value ($<\frac{1}{4}$) at a finite time. After this instant of time, the $\beta_{\langle R\rangle}$ increases to reach the asymptotic

value of $\frac{1}{4}$ at infinite time. The early regime with $\beta_{\langle R\rangle} > \frac{1}{4}$ is dominated by the breakdown of the Young-Laplace model Eq. (5.44) induced by long range forces. On the other side, the late time regime with $\beta_{\langle \mathrm{R}\rangle} < \frac{1}{4}$ is dominated by the screening length effects discussed in Sec. V E [see Eq. (5.54) and the last paragraph of Sec. V E]. Thus, at the longest times, the $\beta_{\langle \mathrm{R}\rangle}$ ultimately approaches $\frac{1}{4}$ *from below*; see Fig. 15. Due to the same reason (i.e., the competition between long range forces and screening length effects), the exponents $\beta_{\langle V\rangle}$ and $\beta_{\langle H\rangle}$ also exhibit nonmonotonous time evolution and they cross their asymptotic values at finite times, as evidenced by our analytic results for these exponents in Fig. 15. On the other hand, there is no such finite time crossing for the pressure exponent $\beta_{\langle P\rangle}$, as evidenced by our analytic results in Fig. 15, showing that this exponent monotonously approaches its asymptotic value from above [for the reason discussed in the last paragraph of Sec. V E]. All these analytic conclusions are consistent with the corresponding simulation results of Sec. III.

VI. SUMMARY

In summary, we presented the following.

(i) We discussed a generalized Mullins model for dewetting of solid films.

(ii) We used numerical simulations of the model to explore the role played by the long range dewetting interactions on the character of the cluster coarsening dynamics.

(iii) We find that these interactions produce significant early time departures from the asymptotic predictions based on the classical Young-Laplace model.

(iv) To address this phenomenon, we first provided a theoretical description of quasistatic (slowly evolving) clusters that goes beyond the classical Young-Laplace model.

(v) Next, we used this description to develop a powerful cluster dynamics theory capable of calculating effective coarsening exponents and thus analytically explain the findings of our simulations.

We have theoretically proved, by numerical simulations and analytic methods, that the long range nature of dewetting forces produces long lasting early time departures from the asymptotic (Young-Laplace) power laws, with the early time effective exponent $\beta_{\langle H\rangle} > 0.25$ for the growth of cluster height. Experimentally, such an effective early time exponent, measured to be $\beta_{\langle H\rangle} \approx 0.33$, has been indeed reported in Ref. [13]. Our analytic theory, in combination with simulations, explains these experimental findings in terms of long range dewetting potentials such as van der Waals attraction.

We recall that the above results apply for the case of *initially* very thin films (with a few monolayers or a submonolayer, as in Refs. [13] and [15]). With such initial films, the dominant coarsening mechanism is the diffusive mass transfer between the clusters, whereas the direct cluster coalescence is insignificant. This assertion applies to both solid and liquid very thin films. Related to this, as discussed in Sec. II E, our results for the cluster size-dependent coarsening exponents in the generalized Mullins model (for solid films) are also applicable to the liquid clusters, as in the experiments of Ref. [13]. On the other side, for initially thick films (with many monolayers), cluster coalescence will become significant, and we anticipate significant differences between solid and liquid films. An analytic theory of the cluster coarsening growth in such thick films remains a challenge for future studies.

Finally, we would like to stress that the present study highlights the physical significance of the early time coarsening phenomena characterized by exponents different from those of the late time, asymptotic regime. Much of the previous theoretical (especially analytic) work was really focused on the late time regime, see, e.g., Refs. [9–11,14]. A notable exception is the numerical MC study of Amar *et al.* [36] inspired by an earlier work of Huse [37] on the domain growth in 2D spin exchange kinetic Ising model. Yet, systematic analytic methods capable of treating early time coarsening regimes, such as the methods developed in this study, are scarce in the literature. Early time regimes deserve much more attention. They regularly appear in more complex dynamical systems. In regards to this, an interesting extension of the present study would be to more deeply study the coarsening in the ensembles of aggregates such as fluid membrane vesicles [38], or in other states of soft matter [4,39]. Other venues of potential interest are the complex dynamics of biomolecules adsorbed on surfaces [40] and exotic interfacial dynamics revealed in recent theoretical studies of epitaxial growth [41], to name just a few.

ACKNOWLEDGMENTS

We would like to thank J. Espinosa and D. Lederman for numerous discussions on their experiments.

APPENDIX A

Here we present Young angle calculation for the more general free energy model Eq. (2.7) discussed in Sec. II A, with an h-dependent stiffness $\gamma(h)$. Let us consider the equilibrium film configurations in the limit of zero chemical potential. For them, by Eq. (2.10), in the limit $P \to 0$,

$$-\gamma(h)\vec{\nabla}^2 h - \frac{1}{2}\gamma'(h)(\vec{\nabla}h)^2 + \Phi'_{\mathrm{eff}}(h) = 0. \tag{A1}$$

For films on 1D substrates ($D = 1$), or for one-dimensionally varying interface profiles in any D, Eq. (A1) reduces to

$$\gamma(h)\frac{d^2h}{dx^2} + \frac{1}{2}\gamma'(h)\left(\frac{dh}{dx}\right)^2 - \Phi'_{\mathrm{eff}}(h) = 0. \tag{A2}$$

Next, we note the identity

$$\begin{aligned}\frac{d}{dx}&\left[\frac{\gamma(h)}{2}\left(\frac{dh}{dx}\right)^2 - \Phi_{\mathrm{eff}}(h)\right]\\ &\equiv \gamma(h)\frac{dh}{dx}\frac{d^2h}{dx^2} + \frac{\gamma'(h)}{2}\left(\frac{dh}{dx}\right)^3 - \Phi'_{\mathrm{eff}}(h)\frac{dh}{dx}\\ &\equiv \left[\gamma(h)\frac{d^2h}{dx^2} + \frac{\gamma'(h)}{2}\left(\frac{dh}{dx}\right)^2 - \Phi'_{\mathrm{eff}}(h)\right]\frac{dh}{dx}.\end{aligned} \tag{A3}$$

By Eq. (A2) and the identity (A3) we see that

$$\frac{\gamma(h)}{2}\left(\frac{dh}{dx}\right)^2 - \Phi_{\mathrm{eff}}(h) = C, \tag{A4}$$

where C is an integration constant. Equation (A4) describes a wedge shaped interface profile around the "contact point" of the film with the dry substrate. On the dry side of the contact point, the profile $h(x)$ asymptotically approaches $h_{\min}$. In this limit, by Eq. (A4) we obtain that $C = -\Phi_{\rm eff}(h_{\min}) \equiv -\Phi_{\min} > 0$. With this condition, Eq. (A4) reduces to

$$\frac{\gamma(h)}{2}\left(\frac{dh}{dx}\right)^2 - \Phi_{\rm eff}(h) = -\Phi_{\min}. \tag{A5}$$

On the other (wedge) side of the contact point, $h \to \infty$ for $x \to \infty$. In this limit, $\Phi_{\rm eff}(h \to \infty) \to 0$ and, *also*, the stiffness $\gamma(h \to \infty) \to \gamma$, where $\gamma = \lim_{h\to\infty}\gamma(h)$ is the stiffness of the film-vacuum interface (far away from the contact point). Thus, by Eq. (A5), the interface slope dh/dx approaches the Young angle slope $m_Y = \tan(\theta_Y)$, satisfying the equation

$$\frac{\gamma}{2}(m_Y)^2 - 0 = -\Phi_{\min}. \tag{A6}$$

Equation (A6) is equivalent to Eq. (2.18). By the above derivation of $m_Y = \tan(\theta_Y)$, we arrive at a significant and nontrivial conclusion that the Young contact angle does not depend on the detailed functional form of the height-dependent stiffness $\gamma(h)$. This has not been noted in the classical studies [18].

The result Eq. (A6), i.e., Eq. (2.18) for the Young contact angle actually applies to large clusters in any D. To see this, consider a $D+1$-dimensional cluster on a D-dimensional substrate case ($D = 2$). For a radially symmetric cluster, Eq. (2.10) reduces to

$$\gamma(h)\left[\frac{d^2h}{dr^2} + \frac{D-1}{r}\frac{dh}{dr}\right] + \frac{\gamma'(h)}{2}\left(\frac{dh}{dr}\right)^2 - \Phi'_{\rm eff}(h) = -P. \tag{A7}$$

Around the contact point, we can expand $r = R + x$ with $x \ll R$, where R is the cluster base radius, as in Fig. 12(c). Thus, Eq. (A7) becomes

$$\gamma(h)\left[\frac{d^2h}{dx^2} + \frac{D-1}{R+x}\frac{dh}{dx}\right] + \frac{\gamma'(h)}{2}\left(\frac{dh}{dx}\right)^2 - \Phi'_{\rm eff}(h) = -P. \tag{A8}$$

Expanding, $\frac{1}{R+x} = \frac{1}{R}(1 - \frac{x}{R} + \frac{x^2}{R^2} - \cdots)$ for $x \ll R$, we obtain

$$\gamma(h)\frac{d^2h}{dx^2} + \frac{\gamma'(h)}{2}\left(\frac{dh}{dx}\right)^2 + (D-1)\frac{\gamma}{R}\left(1 - \frac{x}{R} + \frac{x^2}{R^2} - \cdots\right)\frac{dh}{dx} - \Phi'_{\rm eff}(h) = -P. \tag{A9}$$

In the limit of large clusters, $R \to \infty$, the cluster pressure $P \to 0$ (see Sec. II E). In this limit, Eq. (A9) reduces to Eq. (A2) we had for the 1D case. Thus, the result for the contact angle slope $m_Y = \tan(\theta_Y)$ stated in Eq. (A6), i.e., Eq. (2.18) also applies to very large clusters on D-dimensional substrates for any D.

APPENDIX B

Here we discuss the rationale behind Eq. (5.12). Let us consider cluster volume dynamics like in Eq. (5.2), of the form

$$\frac{dV}{dt} = F(V). \tag{B1}$$

Following Lifshits and Slyozov [8], let us consider the scaled volume,

$$x(t) = \frac{V(t)}{V^*(t)}, \tag{B2}$$

where $V^*(t)$ is the zero of $F(V)$, i.e., $F(V^*) = 0$. By (B1) and (B2), one easily obtains

$$\frac{dx}{d\ln(V^*)} = v(x), \tag{B3}$$

with

$$v(x) = \frac{1}{\frac{dV^*}{dt}}F(xV^*) - x. \tag{B4}$$

For the maximum size clusters (with $V = V_{\max}$), $x = x_{\max}$ with, by (B2),

$$x_{\max} = \frac{V_{\max}}{V^*}. \tag{B5}$$

By the arguments put forward by Lifshits and Slyozov [8], the conditions

$$v(x)|_{x=x_{\max}} = 0;\ \left.\frac{\partial v(x)}{\partial x}\right|_{x=x_{\max}} = 0, \tag{B6}$$

have to be satisfied (at long times) to ensure the conservation of the total film volume Eq. (5.6). By (B4) and (B6) one obtains

$$\frac{1}{\frac{dV^*}{dt}}F(x_{\max}V^*) - x_{\max} = 0;\quad \frac{1}{\frac{dV^*}{dt}}V^*F'(x_{\max}V^*) - 1 = 0. \tag{B7}$$

Combining the two relations displayed in (B7) yields the relation,

$$\frac{x_{\max}V^*F'(x_{\max}V^*)}{F(x_{\max}V^*)} = 1, \tag{B8}$$

which is, by (B5), equivalent to

$$\frac{V_{\max}F'(V_{\max})}{F(V_{\max})} = 1. \tag{B9}$$

It is easy to see that (B9) is equivalent to Eq. (5.12). We would like to stress that the above discussion assumes that the cluster ensemble is at long enough time scales such that the relations in (B6) apply. Validity of this assumption is confirmed by the good agreement between our simulation results and the analytic calculations of Sec. V based on the use of (B9), i.e., Eq. (5.12). Indeed, as evidenced by the figures displayed in Sec. V, the analytic calculations and the simulations agree well with each other. The differences between the simulations and analytic calculations seen in these figures at very early times are likely just a transient to the ultimate behavior governed by (B9), i.e., Eq. (5.12). Additionally, the cluster coalescence (not taken into account in the theory of Sec. V) may also contribute to the differences between the theory and the simulations seen at the earliest times; see Sec. II E discussions.

[1] H. B. G. Casimir, Proc. K. Ned. Akad. Wet. **51**, 793 (1948).

[2] E. M. Lifshitz, J. Exp. Theor. Phys. **29**, 94 (1955).

[3] I. E. Dzyaloshinskii, E. M. Lifshitz, and L. P. Pitaevskii, Sov. Phys. JETP **37**, 161 (1960).

[4] J. N. Israelachvili, *Intermolecular and Surface Forces* (Academic Press, London, 1992).

[5] A. Bulgac and A. Wirzba, Phys. Rev. Lett. **87**, 120404 (2001); see also Ref. [27].

[6] A. Wirzba, A. Bulgac, and P. Magierski, J. Phys. A: Math. Gen. **39**, 6815 (2006).

[7] L. V. Mikheev, Sov. Phys. JETP **69**, 358 (1989); A. Ajdari, L. Peliti, and J. Prost, Phys. Rev. Lett. **66**, 1481 (1991).

[8] I. M. Lifshits and V. V. Slyozov, Sov. Phys. JETP **35**, 331 (1959); J. Phys. Chem. Solids **19**, 35 (1961); C. Wagner, Z. Electrochem. **65**, 581 (1961).

[9] A. J. Bray, Adv. Phys. **34**, 357 (1994).

[10] D. Moldovan and L. Golubović, Phys. Rev. Lett. **82**, 2884 (1999); Phys. Rev. E **60**, 4377 (1999); L. Golubović, D. Moldovan, and A. Peredera, Phys. Rev. Lett. **81**,3387(1998); Phys. Rev. E **61**, 1703 (2000).

[11] J. Krug, Adv. Phys. **46**, 139 (1997); Physica A **313**, 47 (2002).

[12] J. W. Cahn and J. E. Hilliard, J. Chem. Phys. **28**, 258 (1958).

[13] M. Zinke-Allmang and L. C. Feldman, Appl. Surf. Sci. **52**, 357 (1991). The initial explanation for the observed early regime with $\beta_{\langle H\rangle}(t) \approx 0.33 > 1/4$ was in terms of the attachment-detachment limited growth. However, as noted by the authors themselves, this mechanism could not provide a satisfactory explanation for the experimental data.

[14] M. Siegert, Phys. Rev. Lett. **81**, 5481 (1998); D. Moldovan and L. Golubović, Phys. Rev. E **61**, 6190 (2000); For a review, see L. Golubović, A. Levandovsky, and D. Moldovan, East Asian J. Appl. Math. **1**, 297 (2011).

[15] M. R. Krause *et al*., J. Vac. Sci. Technol. A **24**, 1480 (2006); For a recent review of solid-state dewetting experimental phenomenology see, C. V. Thompson, Annu. Rev. Mater. Res. **42**, 399 (2012).

[16] B. K. Chakraverty, J. Phys. Chem. Solids **28**, 2401 (1967).

[17] K. Shorlin, S. Krylov, and M. Zinke-Allmang, Physica A **261**, 248 (1998); See also the review of M. Zinke-Allmang, Thin Solid Films **346**, 1 (1999).

[18] P. G. de Gennes, Rev. Mod. Phys. **57**, 827 (1985); F. Brochard-Wyart *et al*., Langmuir **7**, 335 (1991).

[19] C. Favezza, R. Kalynanaraman, and R. Sureshkumar, Nanotechnology **17**, 1536 (2006); H. Krishna *et al*., JOM **60**, 38 (2008).

[20] J. Espinosa, Ph.D. thesis, West Virginia University, 2007, available at http://wvuscholar.wvu.edu; J. Espinosa, H. T. Shi, and D. Lederman, J. Appl. Phys. **99**, 023516 (2006); H. T. Shi, and D. Lederman, Phys. Rev. B **58**, R1778 (1998).

[21] W. W. Mullins, J. Appl. Phys. **28**, 333 (1957); in *Metal Surfaces* (American Society of Metals, Metals Park, OH, 1963), p. 17.

[22] D. J. Srolovitz and S. A. Safran, J. Appl. Phys. **60**, 255 (1986); H. Wong *et al*., Acta Mater. **48**, 1719 (2000).

[23] M. Khenner, Phys. Rev. B **77**, 165414 (2008); **77** 245445 (2008).

[24] R. J. Asaro and W. A. Tiller, Metall. Trans. **3**, 1789 (1972); M. A. Grinfeld, Dokl. Akad. Nauk SSSR **290**, 1358 (1986).

[25] See, e.g., *Heteroepitaxy and Strain*, Matt. Res. Soc. Bull. **21**, Issue 4, edited by L. J. Schowalter (Materials Research Society, Pittsburgh, PA, 1996).

[26] T. C. Lubensky and P. Chaikin, *Principles of Condensed Matter Physics* (Cambridge University Press, Cambridge, UK, 1995), Chap. 10.

[27] M. M. Ozer *et al*., Phys. Rev. B **72**, 113409 (2005); Yu Jia *et al*., *ibid*. **74**, 035433 (2006).

[28] X. Hu, D. G. Cahill, and R. S. Averback, J. Appl. Phys. **89**, 7777 (2001).

[29] A. Vrij, Discuss. Faraday Soc. **42**, 23 (1966); V. S. Mitlin, J. Colloid Interface Sci. **156**, 491 (1993); R. Seeman, S. Herminghaus, and K. Jacobs, Phys. Rev. Lett. **86**, 5534 (2001).

[30] K. B. Glasner and T. P. Witelski, Phys. Rev. E **67**, 016302 (2003); Physica D **209**, 80 (2005); See also, M. B. Gratton and T. P. Witelsky, *ibid*. **238**, 2380 (2009); Phys. Rev. E **77**, 016301 (2008).

[31] F. Otto *et al*., SIAM J. Math. Anal. **38**, 503 (2006).

[32] K. B. Glasner *et al*., Euro. J. Appl. Math. **20**, 1 (2009); K. B. Glasner, SIAM J. Appl. Math. **69**, 473 (2008).

[33] L. Repetto *et al*., Appl. Phys. Lett. **100**, 223113 (2012).

[34] S. Herminghaus *et al*., Science **282**, 916 (1998).

[35] A. J. Ardell, Phys. Rev. B **41**, 2554 (1990).

[36] J. G. Amar, F. E. Sullivan, and R. D. Mountain, Phys. Rev. B **37**, 196 (1988).

[37] D. A. Huse, Phys. Rev. B **34**, 7845 (1986).

[38] L. Golubović and M. Golubović, Phys. Rev. E **56**, 3219 (1997); See also, L. Golubović and T. C. Lubensky, Europhys. Lett. **10**, 513 (1989); L. Golubović, Phys. Rev. E **50**, R2419 (1994).

[39] S. A. Safran, *Statistical Thermodynamics of Surfaces, Interfaces, and Membranes* (Addison-Wesley, Boston, 1994).

[40] M. B. Hochrein *et al*., Phys. Rev. Lett. **96**, 038103 (2006); Phys. Rev. E **75**, 021901 (2007); L. Chen *et al*., Commun. Comp. Phys. **11**, 709 (2012); Int. J. Mol. Sci., **14**, 7932 (2013).

[41] L. Golubović, A. Levandovsky, and D. Moldovan, Phys. Rev. Lett. **89**, 266104 (2002); A. Levandovsky, L. Golubović, and D. Moldovan, Phys. Rev. E **74**, 061601 (2006); A. Levandovsky and L. Golubović, Phys. Rev. B **69**, 241402 (2004); Phys. Rev. E **76**, 041605 (2007); L. Golubović and A. Levandovsky, *ibid*. **77**, 051606 (2008).